J. Fluid Mech. (2008), *vol.* 601, *pp.* 123–164.
doi:10.1017/S0022112008000517 Printed in the United Kingdom

Steady bubble rise and deformation in Newtonian and viscoplastic fluids and conditions for bubble entrapment

J. TSAMOPOULOS, Y. DIMAKOPOULOS, N. CHATZIDAI, G. KARAPETSAS AND M. PAVLIDIS

Laboratory of Computational Fluid Dynamics, Department of Chemical Engineering
University of Patras, Patras 26500, Greece

(Received 7 December 2006 and in revised form 28 November 2007)

We examine the buoyancy-driven rise of a bubble in a Newtonian or a viscoplastic fluid assuming axial symmetry and steady flow. Bubble pressure and rise velocity are determined, respectively, by requiring that its volume remains constant and its centre of mass remains fixed at the centre of the coordinate system. The continuous constitutive model suggested by Papanastasiou is used to describe the viscoplastic behaviour of the material. The flow equations are solved numerically using the mixed finite-element/Galerkin method. The nodal points of the computational mesh are determined by solving a set of elliptic differential equations to follow the often large deformations of the bubble surface. The accuracy of solutions is ascertained by mesh refinement and predictions are in very good agreement with previous experimental and theoretical results for Newtonian fluids. We determine the bubble shape and velocity and the shape of the yield surfaces for a wide range of material properties, expressed in terms of the Bingham $Bn = \tau_y^*/\rho^* g^* R_b^*$, Bond $Bo = \rho^* g^* R_b^{*2}/\gamma^*$ and Archimedes $Ar = \rho^{*2} g^* R_b^{*3}/\mu_o^{*2}$ numbers, where ρ^* is the density, μ_o^* the viscosity, γ^* the surface tension and τ_y^* the yield stress of the material, g^* the gravitational acceleration and R_b^* the radius of a spherical bubble of the same volume. If the fluid is viscoplastic, the material will not be deforming outside a finite region around the bubble and, under certain conditions, it will not be deforming either behind it or around its equatorial plane in contact with the bubble. As Bn increases, the yield surfaces at the bubble equatorial plane and away from the bubble merge and the bubble becomes entrapped. When Bo is small and the bubble cannot deform from the spherical shape the critical Bn is 0.143, i.e. it is a factor of 3/2 higher than the critical Bn for the entrapment of a solid sphere in a Bingham fluid, in direct correspondence with the 3/2 higher terminal velocity of a bubble over that of a sphere under the same buoyancy force in Stokes flow. As Bo increases allowing the bubble to squeeze through the material more easily, the critical Bingham number increases as well, but eventually it reaches an asymptotic value. Ar affects the critical Bn value much less.

1. Introduction

The motion of bubbles in viscous liquids has attracted the interest of many researchers because of its numerous practical applications and scientific challenges. Over many years people have examined the flow and deformation of a single or multiple bubbles theoretically, experimentally and numerically in various flow

fields; see, for example, the reviews by Harper (1972), Clift, Grace & Weber (1978), and Magnaudet & Eames (2000). However, a large number of materials such as suspensions, emulsions, slurries, foams, fermentation broths and polymer solutions deviate from the Newtonian law. These materials are called viscoplastic and their viscosity depends on the local level of stress. The first constitutive law used to describe their behaviour was proposed by Bingham (1922):

$$\boldsymbol{\tau}^* = \left(\mu_o^* + \frac{\tau_y^*}{\dot{\gamma}^*}\right)\dot{\boldsymbol{\gamma}}^* \quad \text{for } \tau^* > \tau_y^*, \tag{1.1a}$$

$$\dot{\boldsymbol{\gamma}}^* = 0 \quad \text{for } \tau^* \leqslant \tau_y^*, \tag{1.1b}$$

where $\dot{\boldsymbol{\gamma}}^* \equiv \nabla \boldsymbol{v}^* + \nabla \boldsymbol{v}^{*T}$ is the rate of strain tensor and τ^*, and $\dot{\gamma}^*$ are the second invariants of the respective tensors, defined as

$$\tau^* = \left[\tfrac{1}{2}\boldsymbol{\tau}^* : \boldsymbol{\tau}^*\right]^{1/2}, \quad \dot{\gamma}^* = \left[\tfrac{1}{2}\dot{\boldsymbol{\gamma}}^* : \dot{\boldsymbol{\gamma}}^*\right]^{1/2}, \tag{1.2}$$

and μ_o^* and τ_y^* are the plastic viscosity and the yield stress, respectively. The superscript $*$ indicates that the corresponding variable is dimensional. As (1.1) indicate, when the second invariant of the stress exceeds τ_y^*, the material flows with a non-Newtonian viscosity, $\mu_o^* + \tau_y^*/\dot{\gamma}^*$, whereas when it does not exceed it, the material behaves as a solid. The motion of a bubble through a viscoplastic material exhibits new and interesting aspects, which cannot be directly deduced from the corresponding laws for Newtonian liquids. For example, bubbles may become entrapped indefinitely in a viscoplastic material when their buoyancy is sufficiently small compared to τ_y^*, owing to their inability to break the weak physical bonds in the material. However, bubbles may attain shapes that are non-unique, which further complicates the study of their entrapment in a viscoplastic fluid. This behaviour directly affects the quality of a product. For example, aerated chocolate has a taste different from solid chocolate and cosmetic and food products have different appeal and cost depending on the amount of air in them. Also, it affects the efficiency of a physical, chemical or biochemical process. For example, it is more difficult for gases to diffuse from/to an entrapped bubble, slowing down fermentation processes, whereas inside an oil well a gas kick in drilling mud may occur, rise upwards and lead to blowout at the surface (Johnson & White, 1990; Terasaka & Tsuge, 2001; Dubash & Frigaard, 2004, 2006).

Because of the added complexity of a viscoplastic constitutive law and difficulties in observing through such typically opaque materials, the motion of bubbles in them has been studied much less than in Newtonian fluids. A first notable exception is the work of Astarita & Apuzzo (1965) who reported bubble shapes and velocities in viscoplastic (Carbopol solutions) and slightly or highly elastic liquids. They observed that curves of bubble velocity vs. bubble volume for viscoplastic liquids had an abrupt change in slope at a critical value of bubble volume that depended on the concentration of Carbopol in the solution, i.e. the yield stress of the material. The solution concentration also affected the very slow bubble velocities at small bubble volumes and the rate of their increase with bubble volume. The bubble shapes in Carbopol solutions exhibited the usual deformations found in Newtonian fluids, passing from spherical to oblate ellipsoid and finally to spherical caps as their volume increased. Dubash & Frigaard (2007) verified experimentally the observations of Astarita & Apuzzo (1965) on the existence of a critical bubble radius required to set it in motion, but the bubble shapes they observed in different Carbopol solutions inside a vertical pipe were different and resembled an inverted teardrop. Another notable observation was that surface tension significantly affects the bubble stopping conditions. Earlier, the same

authors estimated the conditions under which bubbles should remain static using variational principles (Dubash & Frigaard 2004). The bounds they obtained based on either strain minimization or stress maximization for any type of viscoplastic fluid were characterized as conservative, in the sense that they provide a sufficient but not necessary condition. However, they concluded that in general "if a big bubble does not move nor will a small one". The mobilization of bubbles in a yield-stress fluid by setting them into pulsation was the subject of Stein & Buggish's (2000) research, who presented analytical solutions and experimental data to support them. Apparently larger bubbles rose faster than smaller ones at similar pressure amplitudes. Finally, Terasaka & Tsuge (2001) presented shapes developed by a bubble forming at a nozzle in a yield-stress fluid and provided an approximate model for bubble growth. On the other hand, Dimakopoulos & Tsamopoulos (2003*a*, 2006) simulated the formation and expansion of a long 'open' bubble during the displacement of viscoplastic liquids by pressurised air from straight, suddenly constricing and expanding cylindrical tubes for a wide range of Bingham (i.e. the dimensionless yield stress) and Reynolds numbers, providing details about the topology of the unyielded regions and their effect on the shape of the long bubble.

The corresponding problem of a solid sphere translating in a Bingham fluid has been studied more extensively. Beris *et al.* (1985) verified earlier estimations, based on variational inequalities, of the dependence of the drag force on the sphere in an unbounded medium as on the yield stress. They solved the governing equations with (1.1) as a constitutive model under creeping flow conditions using an algebraic mapping of the yield surfaces to fixed spherical ones and finite elements. They found that the sphere falls within an envelope of fluid, the shape and location of which depends on the yield stress and that unyielded material arises around the stagnation points of flow at the poles of the sphere. Finally, they obtained the critical yield-stress value beyond which the sphere is immobilized by combining asymptotic scalings derived from the plastic boundary-layer theory with numerical calculations. Similar results have been reported by Liu, Muller & Denn (2002). Blackery & Mitsoulis (1997) extended this study, including the effect of the tube diameter to the sphere diameter ratio when the sphere is moving inside a cylindrical tube, using Papanastasiou's (1987) viscoplastic model. This model holds in both the yielded and unyielded material regions:

$$\boldsymbol{\tau}^* = \left[\mu_o^* + \tau_y^* \frac{1 - \mathrm{e}^{-n\dot{\gamma}^*}}{\dot{\gamma}^*}\right] \dot{\boldsymbol{\gamma}}^*, \tag{1.3}$$

where the stress growth exponent, n, must assume large enough values, depending on the particular flow, in order that the original Bingham model is approached; see Dimakopoulos & Tsamopoulos (2003*a*, 2006) and Burgos, Alexandrou & Entov (1999).

Out of the very extensive literature on bubble motion in viscous liquids, we will mention here only papers that are more relevant to the present work or will be used to compare our predictions to established experimental and theoretical data and demonstrate ways in which the viscoplastic fluids deviate from Newtonian ones. Early on, Haberman & Morton (1954) measured bubble rise velocities as a function of bubble size for various liquids and introduced a new dimensionless number for the description of their results, the Morton number, *Mo*, which depended on the liquid properties only. Hnat & Buckmaster (1976) experimentally determined the physical conditions under which either spherical caps arise or bubbles develop very thin, long and rounded 'skirts' from their sides. Bhaga & Weber (1981) carried

out extensive experiments to determine the physical conditions under which bubbles assume spherical, oblate ellipsoidal, deformed ellipsoidal, spherical cap or skirted shapes, steady or unsteady. They presented these conditions in a map of bubble shapes with the Reynolds vs. Eötvos numbers as parameters. In their photographs of bubble motion in aqueous sugar solutions, they quite clearly visualized the streamlines around and in the wake of these bubbles. Aware of the importance of surface impurities while carrying out experiments with water, Duineveld (1995) used 'hyper clean' water and very accurately determined the velocity and the shape of bubbles, with an equivalent radius of 0.33–1.00 mm or Reynolds numbers in the range $100 \leqslant Re \leqslant 700$. Finally, Maxworthy *et al.* (1996) extended such experiments using clean mixtures of triple-distilled water and pure, reagent grade, glycerine. Hence, they covered a wider range of the relevant parameters and provided plots of the drag coefficient C_d and the bubble terminal velocity versus the diameter of an equal spherical bubble.

The early theoretical studies assumed that the bubble remained spherical in an infinite medium and predicted its drag coefficient under creeping flow conditions (Rybczyński 1911; Hadamard 1911). The corresponding analysis for large but finite Reynolds numbers was first attempted by Levich (1949) who argued that the velocity field around the spherical bubble differed only slightly from the inviscid solution. He evaluated the drag force from energy dissipation based on the irrotational solution, to find that the drag coefficient based on the bubble diameter is $C_d = 48/Re$. Later Moore (1963) performed a very elegant boundary layer analysis to determine the structure of the flow around the bubble and the wake behind it and calculated the next-order correction to this formula. Small bubble deformations in creeping flow were examined by Taylor & Acrivos (1964), who studied the importance of surface tension. Deformation at high Reynolds numbers was examined by Moore (1965), who assumed that the bubble had an oblate spheroidal shape and derived the boundary layer solution for it. Since then, the high-Reynolds-number flow around oblate ellipsoidal bubbles has been examined to investigate among other things the range of Reynolds numbers in which recirculation arises behind the bubble (Blanco & Magnaudet 1995).

Solution of the general problem, depending solely on fluid properties and bubble size and dropping any *a priori* assumption about bubble shape or range of the Reynolds number, demands the use of advanced numerical methods, because of the large and complicated bubble deformations and flow structure around them. This became possible in the middle 1980s. First, Miksis, Vanden-Broeck & Keller (1982) assumed potential flow, included only viscous forces in the normal force balance and calculated shapes of rising bubbles using boundary elements, but inherently flow separation could not be predicted. Then Ryskin & Leal (1984) used finite differences and an orthogonal two-dimensional transformation, to solve the Navier–Stokes equations and obtained bubble shapes for Reynolds numbers up to 200 and Weber numbers up to 18. They also predicted accurately the flow recirculation behind the bubble and suggested that the mechanism of eddy formation behind the bubble is the competition between the rate of vorticity production on the free surface and the rate of vorticity convection downstream. Subsequently, Christov & Volkov (1985) used finite differences with a quite restrictive one-dimensional mapping to obtain such solutions in a narrower parameter range. Numerical methods that do not solve for the bubble shape simultaneously with the flow field, but calculate it *a posteriori* by defining an appropriate function, such as volume tracking and level set, have also been used. Their disadvantage of decreased accuracy can be counterbalanced by their ability to predict more complicated bubble shapes and bubble breakup. Some notable

examples are the papers by Unverdi & Trygvasson (1992), Bonometti & Magnaudet (2006, 2007) and Hua & Lou (2007).

We will solve this free-boundary problem, assuming axial symmetry and steady state, with the very accurate and versatile numerical algorithm that we developed recently for such problems (Dimakopoulos & Tsamopoulos 2003*b*). It is based on a quasi-elliptic set of equations for generating a discretization mesh that conforms to the entire fluid domain outside the bubble. Key ideas for the success of the transformation are limiting the orthogonality requirements on the mesh and employing an improved node distribution function along the deforming boundary through a penalty method. A non-orthogonal mesh is allowed since we will solve the entire equation set by finite elements. The retained orthogonal term eliminates the discontinuous slopes of the coordinate lines that are normal to the free surface. These usually arise owing to the harmonic transformation around highly deforming surfaces. This procedure produces meshes of higher density where necessary: stagnation points of flow, equatorial plane and wake behind the bubble. We have applied this method to a number of free- or moving-boundary steady or transient problems, such as displacement of a Newtonian or viscoelastic fluid from a tube (Dimakopoulos & Tsamopoulos 2003*c*, 2004), transient squeezing of a viscoplastic material between parallel disks (Karapetsas & Tsamopoulos 2006) and deformation of several bubbles during filament stretching (Foteinopoulou *et al.* 2006).

In § 2 we present the governing equations and boundary conditions of this problem. In § 3 we give some basic ideas of our body-fitted coordinate transformation and the key features to implement the finite-element algorithm for solving this problem. We present our results in terms of bubble shapes, yield surfaces, flow structure and conditions for bubble entrapment depending on fluid parameters and bubble size in § 4. Conclusions are drawn in § 5.

2. Problem formulation

We consider the flow of a bubble of volume V_b^* rising at a constant velocity U_b^* through a viscoplastic fluid, with a constant yield stress τ_y^*, and upon yielding a constant dynamic viscosity μ_o^*. We assume axial symmetry and that the fluid is incompressible with constant density ρ^* and a constant interfacial tension with the gas in the bubble γ^*, whereas the viscosity and density of the gas in the bubble are assumed to be zero. Figure 1 illustrates the flow geometry examined herein. The motion of the bubble is driven by gravity which is aligned with the z-axis. We select a reference frame moving with the bubble and locate the origin of the spherical coordinate system at the centre of mass of the bubble. Hence, the bubble becomes stationary and the surrounding fluid moves downwards with velocity $U_f^* = -U_b^*$. Henceforth, we will denote by U^* the magnitude of these velocities.

We scale all lengths with the equivalent radius, R_b^*, of a spherical bubble with the same volume, V_b^*, as the bubble under study: $R_b^* = (3V_b^*/4\pi)^{1/3}$. We scale velocities by balancing buoyancy and viscous forces, i.e. with $\rho^* g^* R_b^{*2}/\mu_o^*$, where g^* is the gravitational acceleration, because: (i) we would like to follow as closely as possible typical experimental procedures which are carried out using the same fluid while varying the bubble size, while the steady rise velocity is measured *a posteriori* and (ii) we would like to determine conditions under which the bubble velocity can approach zero resulting in an entrapped bubble. Then the bubble velocity will be calculated as part of the solution, not imposed beforehand, and will be followed by determination of the values of the dynamic parameters, such as the Reynolds

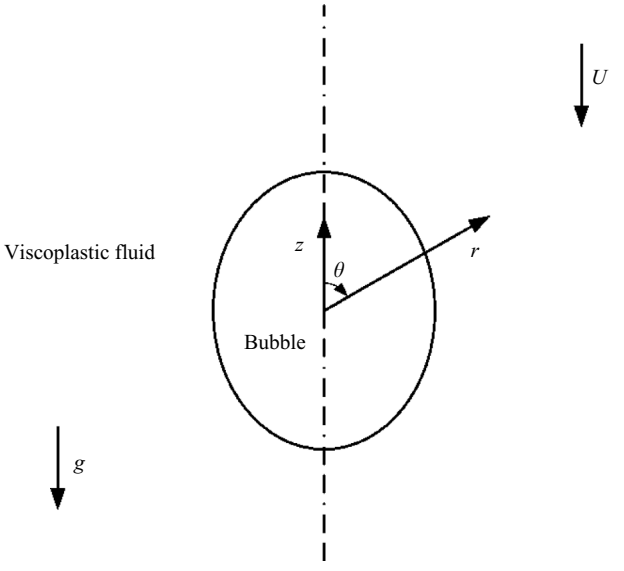

FIGURE 1. Schematic of the flow geometry and coordinate system.

number, $Re = 2R_b^* \rho^* U^* / \mu_o^*$ and the Weber number, $We = 2R_b^* \rho^* U^{*2} / \gamma^*$. Pressure and stresses are scaled with $\rho^* g^* R_b^*$. Thus, the dimensionless groups that arise are the Archimedes number, $Ar = \rho^{*2} g^* R_b^{*3} / \mu_o^{*2}$, which is related to the Galileo number; the Bond number, $Bo = \rho^* g^* R_b^{*2} / \gamma^*$, often called the Eötvos number and the Bingham number, $Bn = \tau_y^* / \rho^* g^* R_b^*$, which is the dimensionless yield stress.

The flow is governed by the momentum and mass conservation equations, which in dimensionless form are

$$Ar\ \boldsymbol{v} \cdot \nabla \boldsymbol{v} - \nabla \cdot \boldsymbol{\sigma} + \boldsymbol{e}_z = 0, \tag{2.1}$$

$$\nabla \cdot \boldsymbol{v} = 0, \tag{2.2}$$

where $\boldsymbol{\sigma}$ is the total stress tensor,

$$\boldsymbol{\sigma} = -P\boldsymbol{I} + \boldsymbol{\tau}, \tag{2.3}$$

$\boldsymbol{v}$ and P are the axisymmetric velocity vector and the pressure respectively, while ∇ denotes the gradient operator. To complete the description, a constitutive equation that describes the rheology of the fluid is required. In the present study we employ the continuous constitutive equation proposed by Papanastasiou (1987) which was mentioned in the introduction and in dimensionless form is

$$\boldsymbol{\tau} = \left[1 + Bn \frac{1 - \mathrm{e}^{-N\dot{\gamma}}}{\dot{\gamma}} \right] \dot{\boldsymbol{\gamma}}, \tag{2.4}$$

where N is the dimensionless stress growth exponent given by $N = n\rho^* g^* R_b^* / \mu_o^*$. In the simulations to be presented in this paper and after careful evaluation, we have chosen the value of N up to 5×10^4 in order to neither affect the yield surface by overly decreasing N nor produce numerical instabilities or stiff equations by increasing it.

Along the free surface of the bubble, the velocity field should satisfy a local force balance between capillary forces, viscous stresses in the liquid and pressure inside the

bubble:

$$\boldsymbol{n}\cdot\boldsymbol{\sigma} = -P_b\boldsymbol{n} + \frac{2H}{Bo}\boldsymbol{n}, \tag{2.5}$$

where P_b is the pressure inside the bubble, $\boldsymbol{n}$ is the outward unit normal to the free surface and $2H$ is its mean curvature which is defined as

$$2H = -\nabla_s\cdot\boldsymbol{n}, \quad \nabla_s = (\boldsymbol{I}-\boldsymbol{nn})\cdot\nabla. \tag{2.6}$$

We cannot define simultaneously both the volume of the bubble and its pressure. Thus, the latter is calculated as part of the solution by imposing that the dimensionless bubble volume remains constant irrespective of bubble deformation and velocity:

$$\int_0^{\pi} R_f^3 \sin\theta \, \mathrm{d}\theta = 2, \tag{2.7}$$

where $R_f(\theta)$ is the radial position of the bubble interface.

On the axis of symmetry ($\theta = 0$ and $\theta = \pi$) we apply the usual symmetry conditions:

$$v_\theta = 0, \tag{2.8}$$

$$\frac{\partial v_r}{\partial\theta} = 0. \tag{2.9}$$

Very far from the bubble, theoretically at infinite distance, the fluid moves in the gravity direction with respect to the stationary bubble and with a uniform dimensionless velocity, U:

$$v_\theta = -U\sin\theta, \tag{2.10}$$

$$v_r = U\cos\theta. \tag{2.11}$$

In our numerical implementation of this condition we will truncate the region around the bubble by a spherical surface at a distance $r = R_\infty$. The value of R_∞ will be determined so that it does not affect the solution. As we will see, this is more crucial for a Newtonian fluid than a viscoplastic one, where the material behaves as a solid at a finite distance from the bubble. The magnitude of the far-field velocity, U, is unknown, but is determined as part of the solution by requiring that the bubble centre of mass remains at the origin of the spherical coordinate system:

$$\int_0^{\pi} R_f^4 \sin\theta\cos\theta \, \mathrm{d}\theta = 0. \tag{2.12}$$

The model is completed by setting the datum pressure of the fluid far from the bubble at the equatorial plane ($r = R_\infty$, $\theta = \pi/2$) equal to zero.

3. Numerical implementation

In order to solve numerically the above set of equations we have chosen the mixed finite element method to discretize the velocity and pressure fields, combined with an elliptic grid generation scheme for the discretization of the deformed physical domain.

3.1. *Elliptic grid generation*

The grid generation scheme that has been employed consists of a system of quasi-elliptic partial differential equations, capable of generating a boundary-fitted discretization of the deforming domain occupied by the liquid; see Dimakopoulos & Tsamopoulos (2003*b*). There it was shown that this scheme is superior to previous ones, since it takes into consideration all the intrinsic features of the developing

surface and the deforming control volume. Here we will only present our adaptation of its essential features to the current problem. The interested reader may refer to Dimakopoulos & Tsamopoulos (2003*b*) for further details on all the important issues of the method. With this scheme the physical domain (r, θ) is mapped onto a computational one (ξ, η). A fixed computational mesh is generated in the latter domain while, through the mapping, the corresponding mesh in the physical domain follows its deformations. As computational domain we choose here the volume that would be occupied by the liquid if the bubble remained spherical. This mapping is based on the solution of the following system of quasi-elliptic partial differential equations:

$$\nabla \cdot \left\{ \left(\varepsilon_1 \sqrt{\frac{r_\eta^2 + r^2\theta_\eta^2}{r_\xi^2 + r^2\theta_\xi^2}} + (1 - \varepsilon_1) \right) \nabla \eta \right\} = 0, \tag{3.1}$$

$$\nabla \cdot \nabla \xi = 0, \tag{3.2}$$

where the subscripts denote differentiation with respect to the variable and ε_1 is a parameter that controls the smoothness of the mapping relative to the degree of orthogonality of the mesh lines. This is adjusted by trial and error; here it is set to 0.1. In order to solve the above system of differential equations, appropriate boundary conditions must be imposed. On the fixed boundaries, we impose the equations that define their position, and the remaining degrees of freedom are used for optimally distributing the nodes along these boundaries with the assistance of the penalty method. In addition, along the bubble interface we impose the no-penetration condition:

$$\boldsymbol{n} \cdot \boldsymbol{v} = \boldsymbol{0}, \tag{3.3}$$

together with a condition that imposes the desired distribution of nodes along the free surface.

The computational domain is discretized using triangular elements by appropriately splitting into two triangular elements each rectangular element generated by our mesh generation method. This splitting is preferred, because triangles conform better to large deformations of the physical domain and can sustain larger distortions than the rectangular ones. In order to illustrate the quality of the mesh produced following our method we present in figure 2*a* a blowup of the physical domain close to the bubble, along with the entire mesh around the bubble in figure 2*b*. For clarity in this figure, we show the nearly rectangular elements before splitting them into triangular ones in a case with only 80 radial and 90 azimuthal elements. As we can see, the mesh becomes smoothly denser where this is most needed, around the bubble surface and near its equatorial plane and its poles, because unyielded regions or flow recirculation are expected to arise there. In order to compute accurately the large deformations of the physical domain, even under the axial symmetry assumption, we used, in most cases, the type of mesh shown in figure 2*b*, but with 120 elements on the ξ-direction (radial) and 100 elements on the η-direction (azimuthal), resulting in 24 000 triangular elements and 205 985 unknowns including the two coordinates of each grid point. An alternative mesh that was employed in order to use the highest value of the stress growth exponent (5×10^4), without running into numerical problems, is shown in figure 2*c*. Here we started with 70 radial and 50 azimuthal equidistant elements far away from the bubble, but for $2 \leqslant \xi \leqslant 3$ we split each rectangle into four rectangles using a strip of rectangle elements around the bubble that were split to three transition triangular elements to connect the two regions. In this way we quadruple the elements

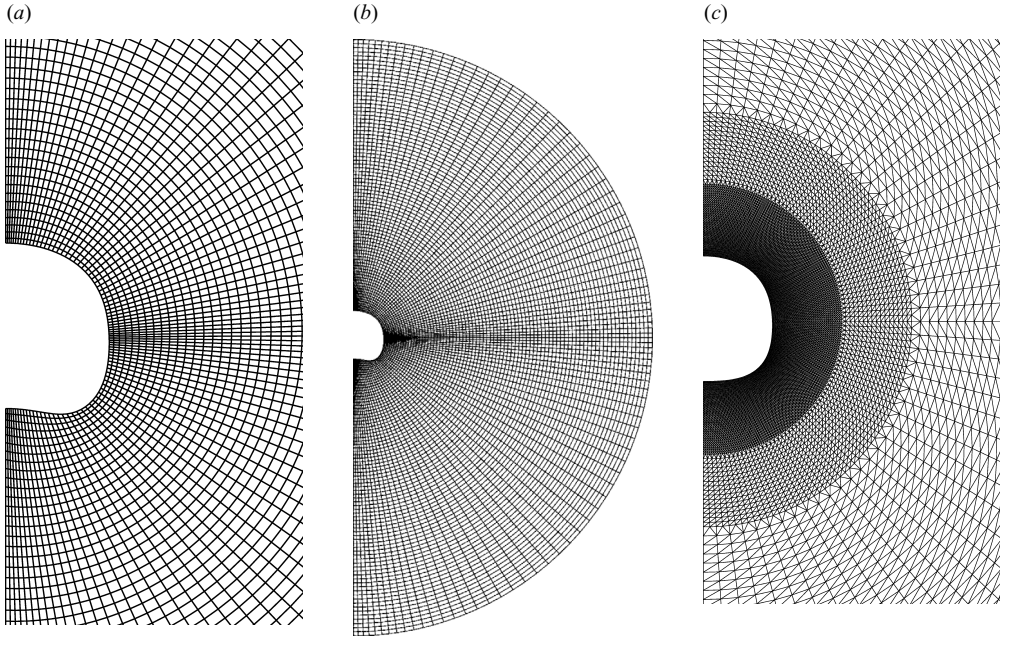

FIGURE 2. Typical mesh, always conforming to the bubble boundary, for $Bn = 0.1$, $Ar = 500$, $Bo = 50$. For clarity we show rectangular elements only and (*a*) a region near the bubble and (*b*) the entire physical domain which in this case extends to $R_\infty = 10$. (*c*) Alternative mesh for the highest value of the stress growth component, showing triangular elements.

in both ξ- and η-directions. We perform another similar refinement through element splitting in the region $1 \leqslant \xi \leqslant 2$. In this way we achieved a much finer mesh near the bubble where it is most needed as we will see shortly, while we actually reduced the computational time and computer memory requirements. For example, at the bubble surface this approach results in 200 elements in the azimuthal direction, while the total number of unknowns has now decreased to 185 223, although the mesh is denser near and all around the bubble and in both directions. With both mesh generation methods, we ensured that there were at least two mesh nodes in any thin boundary layer that could arise at the bubble surface at large Reynolds numbers, as discussed by Blanco & Magnaudet (1995).

3.2. *Mixed finite element method*

We approximate the velocity vector as well as the position vector with 6-node Lagrangian basis functions, ϕ^i, and the pressure with 3-node Lagrangian basis functions, ψ^i. We employ the finite element/Galerkin method, which after applying the divergence theorem results in the following weak forms of the momentum and mass balances:

$$\int_\Omega [Ar\ \boldsymbol{v}\cdot\nabla\boldsymbol{v}\phi^i + \nabla\phi^i\cdot\boldsymbol{\sigma} + \phi^i\boldsymbol{e}_z]\,\mathrm{d}\Omega - \int_\Gamma [\boldsymbol{n}\cdot\boldsymbol{\sigma}]\phi^i\,\mathrm{d}\Gamma = 0, \tag{3.4}$$

$$\int_\Omega \psi^i \nabla\cdot\boldsymbol{v}\,\mathrm{d}\Omega = 0, \tag{3.5}$$

where $\mathrm{d}\Omega$ and $\mathrm{d}\Gamma$ are the differential volume and surface area respectively. The surface integral that appears in the momentum equation is split into four parts, each one corresponding to a boundary of the physical domain, and the relevant boundary

condition is applied. In order to avoid dealing with the second-order derivatives that arise in the boundary integral of the interface, through the definition of the mean curvature, H, we use the following equivalent form:

$$2H\boldsymbol{n} = \frac{\mathrm{d}\boldsymbol{t}}{\mathrm{d}s} - \frac{\boldsymbol{n}}{R_2}, \tag{3.6}$$

where the first term describes the change of the tangential vector along the free surface, $\boldsymbol{t}$, and R_2 is the second principal radius of curvature, $R_2 = r\sqrt{r^2\theta_\eta^2 + r_\eta^2}/(r\theta_\eta - r_\eta \cot\theta)$. The weak form of the mesh generation equations is derived similarly by applying the divergence theorem:

$$\int_\Omega \left(\varepsilon_1 \sqrt{\frac{r_\eta^2 + r^2\theta_\eta^2}{r_\xi^2 + r^2\theta_\xi^2}} + (1-\varepsilon_1) \right) \nabla\eta \cdot \nabla\phi^i \, \mathrm{d}\Omega + L \int_\Gamma \frac{\partial \phi^i}{\partial \eta} \sqrt{r_\eta^2 + r^2\theta_\eta^2} \, \mathrm{d}\eta = 0, \tag{3.7}$$

$$\int_\Omega \nabla\xi \cdot \nabla\phi^i \, \mathrm{d}\Omega = 0, \tag{3.8}$$

where the penalty parameter, L, is in the range 10^3–10^5 and the line integral is along the free surface.

The resulting set of algebraic equations is solved simultaneously for all variables using the Newton–Raphson method. The Jacobian matrix that results after each Newton iteration is stored in Compressed Sparse Row (CSR) format and the linearized system is solved by Gaussian elimination using PARDISO, a robust, direct, sparse-matrix solver, Schenk & Gärtner (2004, 2006). The iterations of the Newton–Raphson method are terminated using a tolerance for the absolute error of the residual vector, which is set at 10^{-9}. The code was written in Fortran 90 and was run on a workstation with dual-core Xeon CPU at 2.8 GHz in the laboratory of Computational Fluid Dynamics, Patras. Each calculation typically required 2–5 hours to complete.

3.3. *Yield surface determination*

There are two criteria that have been employed by several researchers in the past for determining the location of the yield surface: the first as the location where $\dot{\gamma}^* = 0$, and the second as the location where $\tau^* = \tau_y^*$. Although these criteria are equivalent according to the Bingham model, they are not equivalent when the Papanastasiou model is used. In fact, only the second criterion may be used, i.e. that the material flows when the second invariant of the extra stress tensor exceeds the yield stress. This criterion in its dimensionless form becomes

$$\text{yielded material:} \qquad \tau > Bn, \tag{3.9}$$

$$\text{unyielded material:} \qquad \tau \leqslant Bn. \tag{3.10}$$

Near the yield surface, i.e. for small $\dot{\gamma}$, this is equivalent to

$$\dot{\gamma} \approx \frac{Bn}{1 + NBn} \to \frac{1}{N},$$

for large N values, which should substitute the first criterion as shown by Dimakopoulos & Tsamopoulos (2003*a*).

Consequently, in order to determine the yield surface, the second invariant of the stress tensor must be calculated and this includes the computation of the velocity gradient tensor. As mentioned earlier however, the velocity field is discretized using Lagrangian basis functions, which means that the velocity gradient tensor is not

	$\rho^*(\mathrm{kg\,m^{-3}})$	$\eta_o^*(\mathrm{N\,s\,m^{-2}})$	$\sigma^*(\mathrm{N\,m^{-1}})$	*Mo*
a	1000	10^{-3}	0.0727	2.722×10^{-11}
b	1153.8	9.45×10^{-3}	0.06782	2.174×10^{-7}
c	1208.5	0.0601	0.0655	3.769×10^{-4}

TABLE 1. Physical properties of experimental data by Maxworthy *et al.* (1996).

continuous on the element sides and, hence, direct computation at the nodes of the stress tensor is not possible. The most appropriate way to do this is to find a continuous approximation of the extra stress tensor by using the Galerkin projection method, that is

$$\int_{\Omega} \phi^i \, (\boldsymbol{T} - \boldsymbol{\tau}) \, \mathrm{d}\Omega = 0, \tag{3.11}$$

where $\boldsymbol{T}$ denotes the continuous approximation of the extra stress tensor $\boldsymbol{\tau}$. Having calculated the nodal values of the extra stress tensor, the position of the yield surface can be easily determined. A similar procedure is followed to obtain contour lines of $\dot{\gamma}$.

4. Results and discussion

First we will demonstrate that our numerical algorithm predicts accurately bubble shapes and velocities and flow field structure of earlier studies. Such detailed studies exist only for Newtonian fluids. In the process, we will show that our algorithm can extend the parameter values for which converged and accurate solutions have been obtained even for Newtonian fluids. Then, we will present results for bubble rise velocity, deformation and entrapment in a viscoplastic fluid depending on the fluid parameters and bubble volume. All our results are based on the assumptions of axial symmetry and steady state. Clearly, obtaining such a solution does not assure that it is stable; this would require a separate stability analysis. Conversely, not obtaining such a solution does not imply that a non-axisymmetric or time-dependent solution does not exist, for the same parameter values.

4.1. *Comparison with previous experimental and numerical results for Newtonian fluids*

First, we compare our results with the experimental observations by Duineveld (1995) who measured bubble rise velocities as a function of bubble size in 'hyper clean' water and by Maxworthy *et al.* (1996) who conducted the same experiments using mixtures of distilled water with glycerin to produce more viscous liquids. The physical properties of these liquids are shown in table 1. The Morton number, which is given also in table 1, depends only on physical properties of each liquid and is defined as:

$$Mo = \frac{g^* \mu_o^{*4}}{\rho^* \gamma^{*3}} = \frac{Bo^3}{Ar^2}. \tag{4.1}$$

Figure 3 compares our predictions for the rise velocity as a function of bubble diameter with three sets of experimental data, each one related to three values of *Mo*, which cover what are typically called fluids with 'very low' *Mo* values of order 10^{-11} up to fluids with 'high' *Mo* values of order 10^{-4}. In figure 3, d is the diameter in mm of a corresponding spherical bubble of the same volume and U^* is the magnitude of the dimensional rise velocity of the bubble in $\mathrm{mm\,s^{-1}}$. For the two higher values

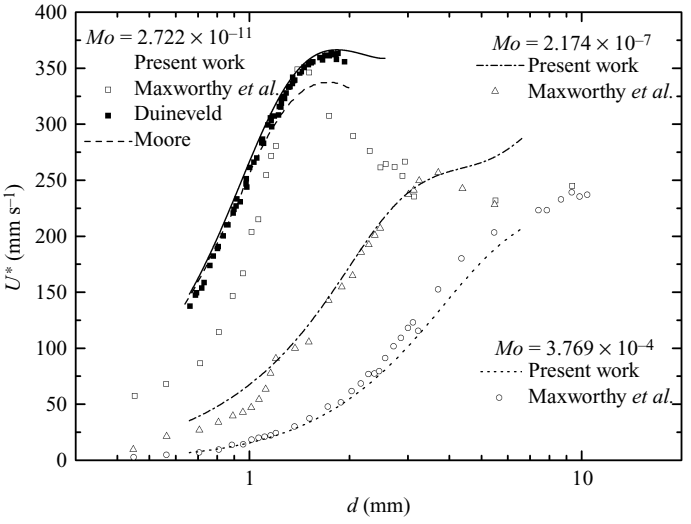

FIGURE 3. Comparison of our predictions for the dimensional bubble rise velocity vs. bubble diameter in a Newtonian liquid for three selected values of *Mo* with experiments reported by Duineveld (1995), Maxworthy *et al.* (1996) and theory by Moore (1965).

of *Mo*, which correspond to more viscous fluids, we observe very good agreement between our predictions and the data of Maxworthy *et al.* (1996). For the lowest value, $Mo = 2.722 \times 10^{-11}$, attained using pure water, we have excellent agreement between our predictions and the experimental data of Duineveld (1995). Even Moore's (1965) analytical predictions, based on the assumptions that the bubble retains an oblate spheroidal shape and that non-separated flow takes place that can be calculated using boundary layer analysis, are in excellent agreement, except for the largest bubbles where bubble shapes deviate from the assumed symmetric shape and flow separation becomes possible. On the other hand, bubble velocities measured by Maxworthy *et al.* (1996) are consistently lower, especially for the smaller bubbles. This has been attributed by Maxworthy *et al.* (1996) to a very small amount of impurities that is still present in their fluids, which is known to affect the smaller bubbles more substantially. For all values of *Mo* we observe that, as the size of the bubble increases from its smallest value, its rise velocity increases, owing to the increased buoyancy. The less viscous the liquid, the higher the rise velocity is, as the resistance to flow decreases. Moreover, the rate of increase of U^* is larger for the fluid with the smallest *Mo*. In the same fluid with $Mo = 2.7 \times 10^{-11}$, a maximum velocity is achieved at a certain bubble size, beyond which the velocity decreases and, then, it increases again. The interplay of the forces on the bubble for different sections of this curve has been analysed by Maxworthy *et al.* (1996). The maximum in the bubble velocity vs. bubble diameter corresponds to the minimum in a drag coefficient vs. Reynolds number curve that has been reported for these and other low-*Mo* fluids in the literature. The shape of this curve becomes for large *Mo*, exactly as we predict in figure 3. For the lower bubble diameters for all three curves the bubbles are nearly spherical. As the bubble diameter increases, they first become oblate spheroidal and then asymmetric having a flatter front side in the two curves with lower *Mo* or a flatter rear side for the curve with the highest *Mo*.

In figure 4 we compare the predictions of our simulations to the experimental observations of Duineveld (1995) for the Weber number dependence of the bubble

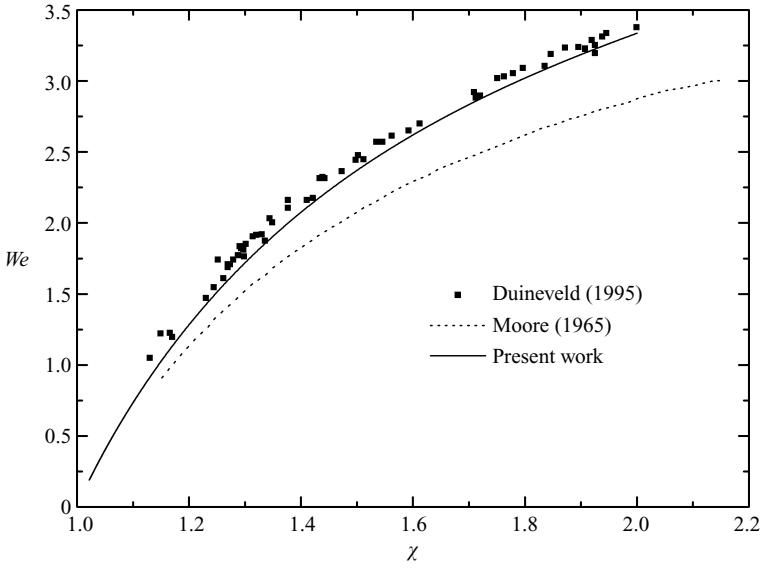

FIGURE 4. Comparison of our predictions for *We* vs. bubble aspect ratio, χ, in pure water with results by Duinevelt (1995) and Moore (1965).

deformation expressed by the ratio between the longer and smaller axes of the bubble, χ. In both the experiments and our study, *We* can be obtained after computing the magnitude of the bubble rise velocity, U, since it is related to it and the dimensionless numbers we have defined by the expression

$$We = \frac{2R_b^* \rho^* U^{*2}}{\gamma^*} = 2Ar\, Bo\, U^2. \tag{4.2}$$

Clearly, numerical and experimental results are in excellent agreement. In the same figure, we include Moore's predictions, which require a consistently larger bubble deformation for a given *We* (i.e. bubble rise velocity) owing to their inability to predict flow separation.

To further validate our new algorithm we compared the predicted drag coefficient for a steadily rising bubble with that calculated by Ryskin & Leal (1984, referred to herein as RL) for different values of *Re* and *We*. The Reynolds number and the drag coefficient are defined as

$$Re = \frac{2R_b^* \rho^* U^*}{\mu_o^*} = 2Ar\, U, \tag{4.3}$$

$$C_d = \frac{2F^*}{\rho^* U^{*2} \pi R_b^{*2}} = \frac{2F}{\pi Ar\, U^2}, \tag{4.4}$$

where F is the dimensionless drag force, defined in terms of $\boldsymbol{\tau}$ and the dynamic pressure, P_{dyn}:

$$F = 2\pi \int_0^{\pi} \boldsymbol{n} \cdot (-P_{dyn}\boldsymbol{I} + \boldsymbol{\tau}) \cdot \boldsymbol{e}_z R_f^2 \sin\theta \, \mathrm{d}\theta, \tag{4.5}$$

where P_{dyn} includes the gravitational potential. Having calculated the magnitude of the bubble velocity, U, we readily determine the values of C_d, *Re* and *We*. However, it is not obvious how to obtain the same parameter values for *Re* and *We* as those reported by RL. To this end, we had to rely on trial and error, choosing values

Re	We	C_d (Present work)	C_d (Ryskin & Leal)
1	0.003	17.43	17.35
10	0.02	2.39	2.38
20	15	3.53	3.57
100	2.1	0.53	0.54
101	0.14	0.37	0.39

TABLE 2. Comparison of the drag coefficient calculated herein to that calculated in RL.

$Bo\backslash Ar$	0.01	0.1	1	5	10	20	40	50
1	10^{-6}	10^{-3}	1	125	10^{3}	8×10^{3}	6.4×10^{4}	1.25×10^{5}
5	4×10^{-8}	4×10^{-5}	0.04	1	40	320	2.56×10^{3}	5×10^{3}
50	4×10^{-10}	4×10^{-6}	4×10^{-4}	2×10^{-3}	0.4	3.2	25.6	50
500	4×10^{-12}	4×10^{-9}	4×10^{-6}	5×10^{-4}	4×10^{-3}	0.032	0.256	0.5
5000	4×10^{-14}	4×10^{-11}	4×10^{-8}	5×10^{-6}	4×10^{-5}	3.2×10^{-4}	2.56×10^{-3}	5×10^{-3}

TABLE 3. Morton number for the values of Archimedes and Bond numbers shown in figures 5 and 10.

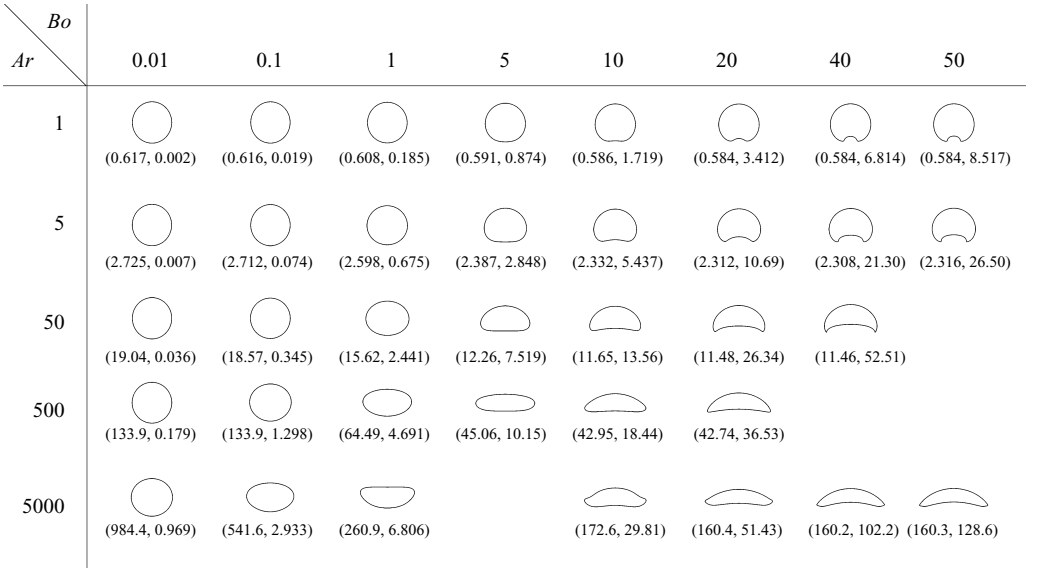

FIGURE 5. Map of bubble shapes in a Newtonian fluid as a function of the Bond and Archimedes numbers. Underneath each figure we give the corresponding Reynolds and Weber numbers (Re, We).

of Ar and Bo, to prepare table 2, which demonstrates that the drag coefficients we calculated are in very good agreement with those of RL and, in this range of Re, they decrease with it.

To set the stage for the presentation of bubble shapes in viscoplastic fluids, it is useful to examine first the effect of fluid properties and bubble size on the shape of the bubble when it is steadily rising in a Newtonian fluid. In figure 5 we show a map of bubble shapes as a function of Bo and Ar. The corresponding Mo is given in table 3 and remains the same in the similar shape maps of bubbles in Bingham fluids, to be

presented in § 4.2. For easy reference and comparison to previous studies, underneath each shape we give the corresponding *Re* and *We*. We have obtained steady solutions for $4 \times 10^{-14} \leqslant Mo \leqslant 1.25 \times 10^{5}$ which is a much wider range of *Mo* than has been available up to now, and for *Bo* as high as 50. Results for $Ar = 0$ and any *Bo* are not shown, because according to (4.2) and (4.3), this leads to $Re = We = 0$ and, of course, to a perfectly spherical bubble in a Newtonian fluid; see also RL. However, as *Ar* and *Bo* increase, the importance of gravitational and inertia forces increases and affects the shape of the bubble. For $Ar \leqslant 500$, on increasing *Bo*, the shape of the gas bubble changes from spherical to oblate-spheroid and to more complicated 'oblate' shapes with an indentation and/or flattening of their rear side. For $Bo \geqslant 20$, it seems that for the same *Ar* the overall shapes do not change much, except that they become more pointed at their rim. It is known that for even higher values of *Bo*, skirted bubbles develop, which demand a much finer discretization. For $Ar = 5000$, on increasing *Bo*, the bubble first flattens at its top side, then for $3.7 \leqslant Bo \leqslant 8.8$ steady solutions could not be obtained with this procedure. The shape we managed to compute for $Bo = 10$ is obtained by parameter continuation in *Ar*, not by increasing *Bo*. It required special attention to be captured accurately. In particular, we had to remove the outer boundary very far away from the bubble in order not to affect the flow in any way, $R_{\infty} = 100$, and we had to increase the radial elements to 180, while keeping the azimuthal elements at 100 with the mesh shown in figure 2(*b*). This steady shape is qualitatively different from all others reported heretofore, exhibiting an upward indentation of the bubble outer edge and flatter rear side, resembling a hat. As we start to increase *Bo*, the bubble becomes a spherical cap again. Comparing our bubble shapes for various *Re* and *We* when such shapes are also available in RL we find very good agreement. We should mention that we managed to compute steady bubble shapes for larger *Re* and *We* than in RL. For example, $Ar = 5000$ and $Bo = 0.01$ correspond to $Re = 984$ and $We = 0.97$, while $Ar = 50$ and $Bo = 20$ correspond to $Re = 43$ and $We = 36.5$. We had no difficulty in reaching even higher values of *Ar*, but it is known that, beyond critical values of *Re* and *We*, time-dependent solutions prevail.

We have captured accurately not only the bubble shapes, but also the details of the flow around them and the recirculation behind them, as shown in figure 6, which compares the experimental observations in Hnat & Buckmaster (1796, referred to herein as HB), left-hand side of each plot, to our predictions, right-hand side, for three cases given in that reference. In all three cases of spherical-cap shapes, these shapes and the streamline pattern including flow separation and wake formation compare extremely well. This flow separation from a smooth fluid/fluid interface has now been reported in numerous theoretical and numerical studies, e.g. RL and HB. The indentation in the rear of the bubble is not visible in the photograph by HB, but can be visualized by the dotted line we have drawn from the bubble tip towards the axis of symmetry in our results. A larger indentation in the rear of the bubble appears in figure 7, which compares our predictions to the experimental observations by Bhaga & Weber (1981, referred to herein as BW), who unfortunately did not show streamlines. Again the agreement is extremely good. The excellent agreement holds for $5 \times 10^{-3} \leqslant Mo \leqslant 10^{3}$ and *Re* up to ~ 100, which is the entire range reported by BW. This is shown in figure 8 where we compare some of the geometric characteristics of the flow concerning bubble and wake shapes to our predictions. These characteristics were introduced and measured by BW and are defined in figure 8(*a*). In figure 8(*b*), we clearly see that increasing *Re* increases the bubble width and in figure 8(*c*) that it decreses the bubble height for the entire range of Morton numbers shown. Moreover,

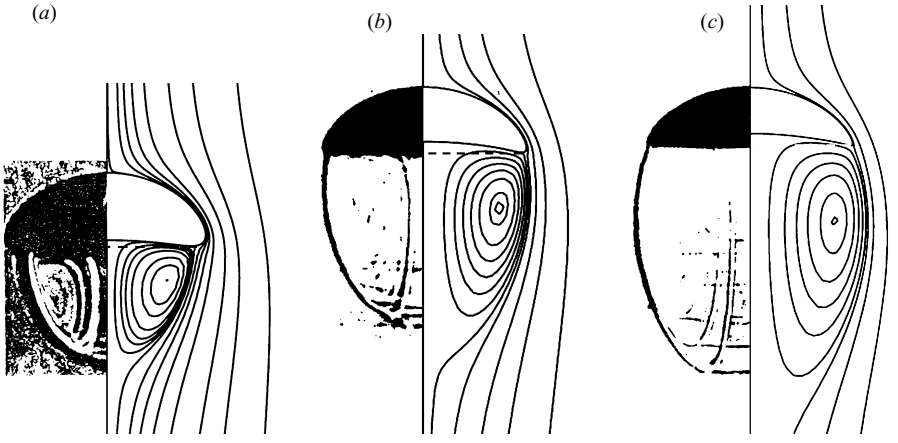

FIGURE 6. Comparison of bubble shapes and flow streamlines observed by HB (left half) with our predictions (right half): (*a*) $Re = 19.62$, $We = 15.64$, (*b*) $Re = 32.69$, $We = 31.72$ and (*c*) $Re = 50.18$, $We = 58.04$.

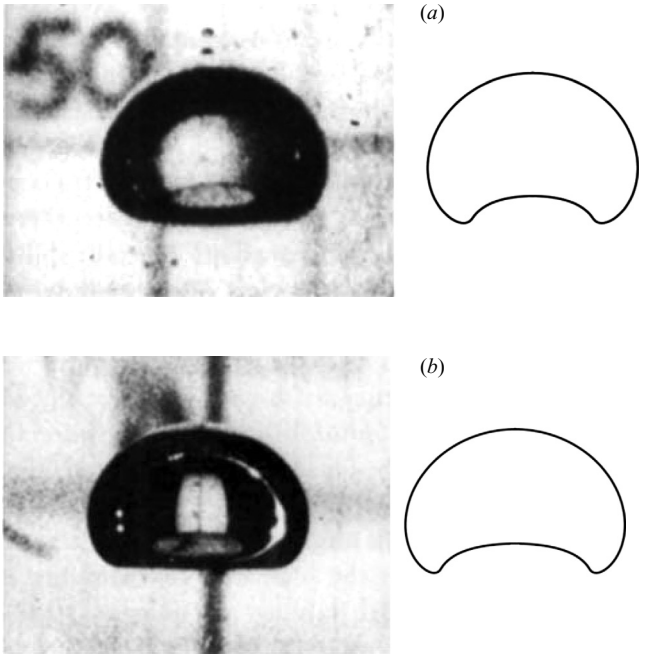

FIGURE 7. Comparison of bubble shapes observed by BW on the left with our predictions on the right: (*a*) $Re = 2.44$, $We = 16.11$ and (*b*) $Re = 3.78$, $We = 21.69$.

increasing Re increases both the width (figure 8*d*) and length (figure 8*e*) of the wake and moves its centre behind the bubble further away from the bubble (figure 8*f*).

4.2. *Bubble shapes in Bingham fluids*

First, we will present some of the convergence tests we have performed to verify that our results have converged with the exponent N of the Papanastasiou model. We have also undertaken the usual convergence tests with just mesh refinement, but we will not report them here for conciseness. The issue of convergence of

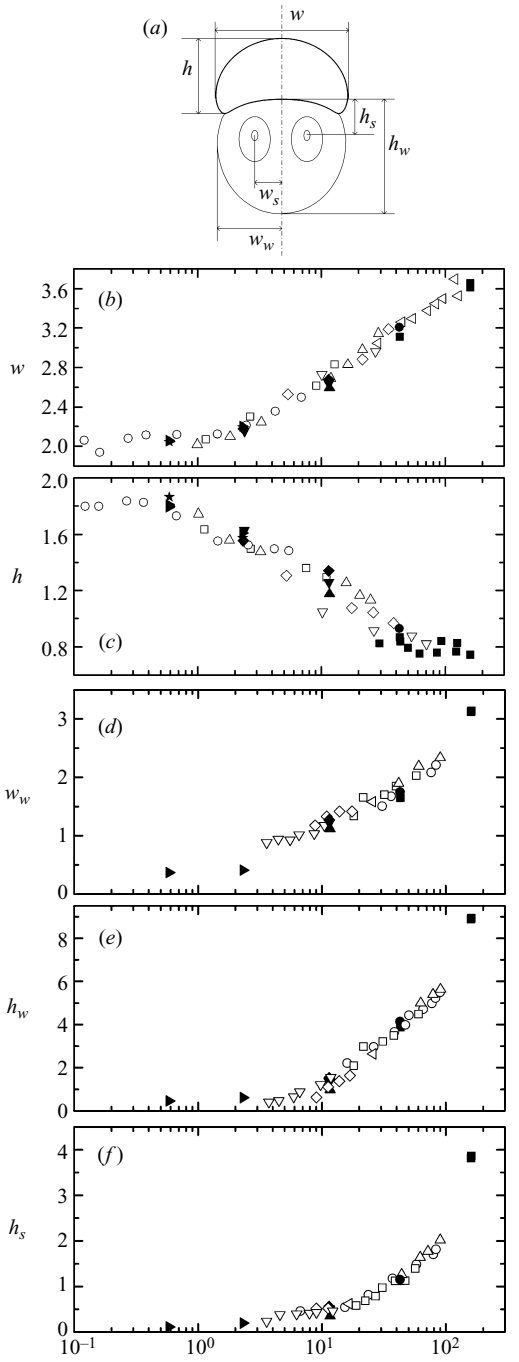

FIGURE 8. Geometric characteristics of the bubble and the vortex behind it as observed in the experiments by BW (open symbols) and predicted by our code (filled symbols) as a function of Re: (a) definitions of bubble characteristics, (b) dimensionless width of the bubble, (c) dimensionless height of the bubble, (d) dimensionless width of the vortex, w_w, (e) dimensionless height of the vortex, h_w, and (f) dimensionless location of the stagnation ring of the vortex, h_s. (BW: ○, $Mo = 711$; □, $Mo = 55.5$; △, $Mo = 4.17$; ◇, $Mo = 1.03$; ▽, $Mo = 0.108$; ◁, $Mo = 5.48 \times 10^{-3}$. Present work: ■, $Mo = 2.5 \times 10^{-3} - 5 \times 10^{-3}$; ●, $Mo = 3.2 \times 10^{-2}$; ▲, $Mo = 0.4$; ▼, $Mo = 1,\ 3.2$; ◆, $Mo = 25.6,\ 40$; ★, $Mo = 125,\ 320$, ► $Mo = 10^{3} - 1.25 \times 10^{5}$).

Variable	v_r	v_θ	τ_{rr}	$\tau_{r\theta}$	$\tau_{\theta\theta}$	P
Case B_1	−0.685	−0.689	−0.648	−0.635	−0.598	−0.502
	(1.3×10^{-5})	(1.5×10^{-5})	(5.2×10^{-5})	(3.6×10^{-5})	(3.0×10^{-5})	(2.3×10^{-5})
Case B_2	−0.867	−0.870	−0.721	−0.751	−0.584	−0.701
	(7.4×10^{-6})	(8.2×10^{-6})	(3.9×10^{-5})	(3.0×10^{-5})	(1.9×10^{-5})	(1.1×10^{-4})

TABLE 4. Least squares fit of the exponents, β, in the expression $\|\text{dev}\| = A\|N\|^{\beta}$, where 'dev' stands for the deviation of the indicated variable of each of the solutions with $N = 100$, 500, 1000 and 5000 from the solution with $N = 10000$. Below each value and in parentheses we give the norm of the 'dev' between the two larger values of N, 5000 and 10000. In case B_1, the parameter values are $Ar = 1$, $Bo = 20$, $Bn = 0.14$ and the mesh has 100 radial and 120 azimuthal nodes, whereas in case B_2 $Ar = 1$, $Bo = 5$, $Bn = 0.1$ and the mesh has 90 radial and 80 azimuthal nodes. In both cases the mesh is of the type shown in figure 2(a, b).

results with N is often raised, when Papanastasiou's or any other of the so-called regularization models are used. All these models depend on some regularization parameter to avoid the discontinuity introduced by the original Bingham model. To verify convergence, Beris *et al.* (1985, referred to herein as BTAB), having modified the discontinuous Bingham model by introducing the regularization parameter suggested by Bercovier & Engelman (1980) and Glowinski, Lions & Trémoliéres (1981), carried out such a convergence study and verified that their results approached an asymptotic value as this regularization parameter reached very large values. Moreover, Smyrnaios & Tsamopoulos (2001) studied the squeeze flow of a Bingham plastic between two parallel disks using either the same regularization parameter as BTAB or Papanastasiou's exponential model. They demonstrated that not did only did each model converge as the each regularization parameter took very large values, but that they converged to the same result. In all cases very sensitive variables for convergence are the rate of strain tensor and the location of the yield surface. On the other hand, Frigaard & Nouar (2005) examined the convergence of regularized models to those of the corresponding exact (discontinuous) model. For the Papanastasiou model they showed that the H_1 norm of the velocity vector converged with increasing N like $N^{-0.5}$, whereas no explicit form was derived for the convergence of the norm of the stress tensor. Nevertheless, it was determined that convergence deteriorated as the second invariant of the stress approached the yield stress, i.e. critical conditions for the entire yielded material. We have carried out repeated tests to verify that the results in this study are independent of the exponent N. One such study is shown in table 4, for two sets of parameters for which we predict that the bubble is about to become entrapped in the material, i.e. near critical conditions, where the velocities have decreased considerably. We calculated the Euclidean norm of the deviation of a solution with $N = 100$, 500, 1000 and 5000 from the solution with $N = 10\,000$ for the velocity and the stress components and the pressure. Here we have used a mesh of the type in figure 2(a, b). We can clearly see that the computations converge with increasing N, faster for the velocities than the stresses or the pressure, with an exponent that is always larger in absolute value than 0.5 and that the difference between values computed with $N = 5000$ and those computed with $N = 10\,000$ is fairly small. Consequently, we can generally consider that our results have converged with N when we take $N = 10\,000$ and that the *a posteriori* calculated yield surfaces are reasonably accurate.

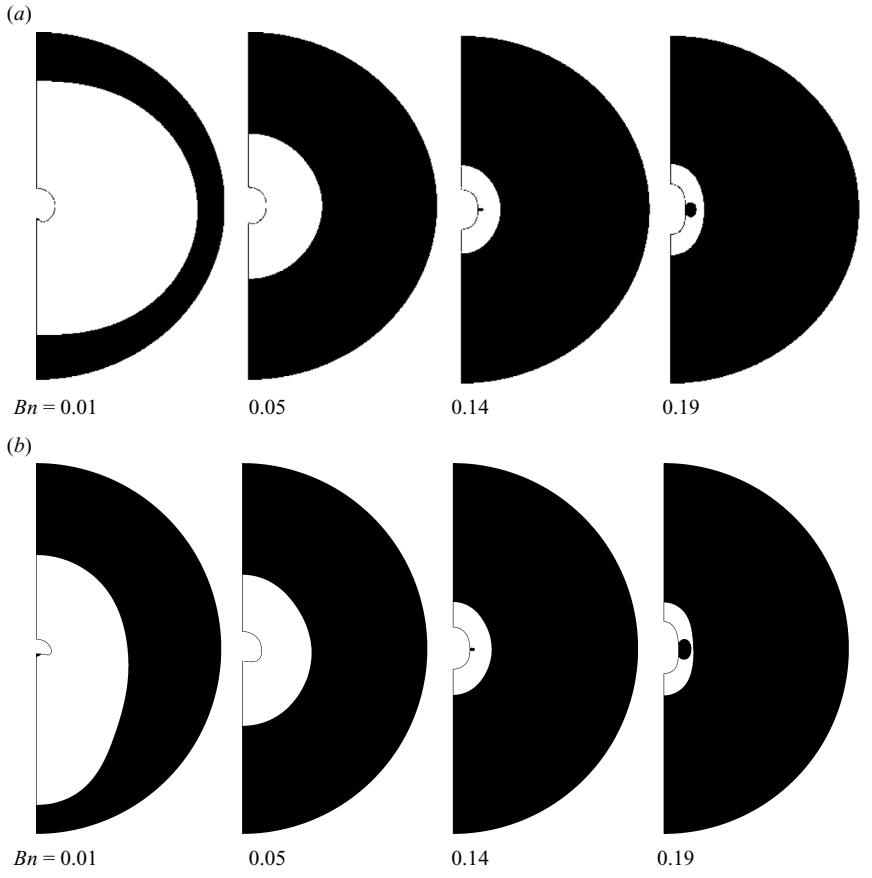

FIGURE 9. Dependence of the bubble shape and the yielded (white) and unyielded (grey) domains on Bn for $N = 10^4$ and (*a*) $Ar = 1$, $Bo = 50$, (*b*) $Ar = 50$, $Bo = 10$, for $Bn = 0.01$, 0.05, 0.14, and 0.19; $R_\infty = 10$ in all cases except for the first one in (*b*) where $R_\infty = 15$.

Next we will discuss the effect of increasing the Bingham number on bubble shapes and yield surfaces. Figure 9 shows the dependence of the bubble shape and the yielded (white) and unyielded regions (grey) on Bn for two quite distinct cases of Ar and Bo. The dimensionless distance of the outer boundary from the bubble centre is always $R_\infty = 10$, except for the first case in figure 9(*b*) where $R_\infty = 15$, in order to include the outer yield surface in each case. In the first set of bubbles (Figure 9*a*), where the gravitational forces balance viscous forces ($Ar = 1$) and capillarity is rather weak ($Bo = 50$) we see that inside the indentation that exists at the rear of the bubble, even for a Newtonian fluid, the stresses fall below the yield stress and a very small region of unyielded material is formed for $Bn = 0.01$. Of course, stresses monotonically decrease away from the bubble and unyielded material exists there also. The yield surface is nearly symmetric around the bubble, but slightly closer to it around the poles. A similar shape of the yield surface was obtained for the creeping flow of a sphere in a Bingham fluid in BTAB. At higher Bn, $Bn = 0.05$, the material around the bubble 'freezes' closer to the bubble surface and the yield surface retains the previously described shape. The bubble elongates a little, and the size of the rear indentation decreases and does not provide enough space for slow enough flow there. Hence the unyielded region at the rear of the bubble disappears. At even

higher Bn ($Bn = 0.14$), the bubble elongates further and unyielded material arises in contact with it around its equatorial plane. BTAB have shown that unyielded material arises around the poles of a solid sphere in a region that increases with Bn. On the contrary in a bubble, the zero-shear-stress condition applied on its entire surface forces it to move with the surrounding liquid. Moreover, bubble deformability makes it elongated-developing a small region around its equatorial plane that is parallel to the z-axis with a locally uniform azimuthal velocity. Around this portion of the bubble surface velocity variations decrease and the material can become unyielded. As Bn increases further, $Bn = 0.19$, the area of the unyielded material at the equatorial plane increases and the unyielded material away from the bubble comes closer to it. Eventually these two unyielded areas will merge, the velocity all around the bubble will drastically decrease and the bubble will be entrapped in the material. We will discuss this further in § 4.4.

In the second case (figure 9*b*) where the gravitational forces are more important compared to viscous forces ($Ar = 50$) and capillarity is not as weak ($Bo = 10$), we observe some distinct changes at small Bn, $Bn = 0.01$ and $Bn = 0.05$, but nearly the same bubble shapes at the larger Bn. At $Bn = 0.01$, the bubble has an oblate ellipsoidal shape with a flatter rear side, not very different from its Newtonian counterpart, but completely different from that in case (*a*). Unyielded material exists at the rear surface of the bubble as in (*a*), but more importantly the rising bubble generates a vortex behind it and enhances the rate of strain there so that unyielded material appears further away from the bubble at its rear than at its front side. Thus, the unyielded surface around the bubble does not have a fore–aft symmetry any longer. At $Bn = 0.05$ the shape of the bubble is still different from that in case (*a*), being flatter underneath, and the unyielded region around the bubble tends to become symmetric. At even higher Bn, both the shape of the bubble and the unyielded areas are much like those in case (*a*).

In figure 10 we show how the map of bubble shapes, given in figure 5, evolves as Bn increases. The corresponding Morton numbers are given in table 3 and the Re and We values underneath each bubble shape. The bubble rise velocity decreases with the Bingham number and that is reflected in the decreasing Reynolds and Weber numbers. We show the unyielded material in grey. For $Bn \leqslant 0.1$ we show only the unyielded material, when it arises, on the bubble surface, because unyielded regions around the bubble are too far away to be included in this figure. For larger Bn we also show the unyielded material around the bubble. Even a small Bn introduces qualitative changes in certain bubble shapes. For example, when $Ar = 0$, $Bn = 0.01$ (figure 10*a*) and Bo is high enough, the bubble is no longer spherical because a small indentation at its rear side has been formed, while when $Bn = 0.05$ (figure 10*b*) and $Bo \geqslant 5$, the shape is again not spherical, but slightly elongated and at its rear side flatter or with a small indentation. Papanastasiou's (and every other) viscoplastic model is nonlinear. This, for finite Bond numbers, i.e. deformable bubbles, the characteristic Newtonian property at $Ar \to 0$ of fore-aft symmetry in the bubble shapes and the flow field is broken. The break-up of the flow fore–aft symmetry in inelastic non-Newtonian fluids has been also experimentally observed in the case of the flow around a settling sphere even at small Reynolds numbers (Gueslin *et al.* 2006). Moreover, the measured rate of strain near the bubble and at the equatorial plane has very small values and consequently the effective viscosity of the material is high there. On the contrary, near the poles the measured rate of strain is higher and the effective viscosity is smaller. As a result, the bubble tends to deform preferentially in the direction of its poles, taking an elongated shape. The elongation of the bubble becomes more prominent as the

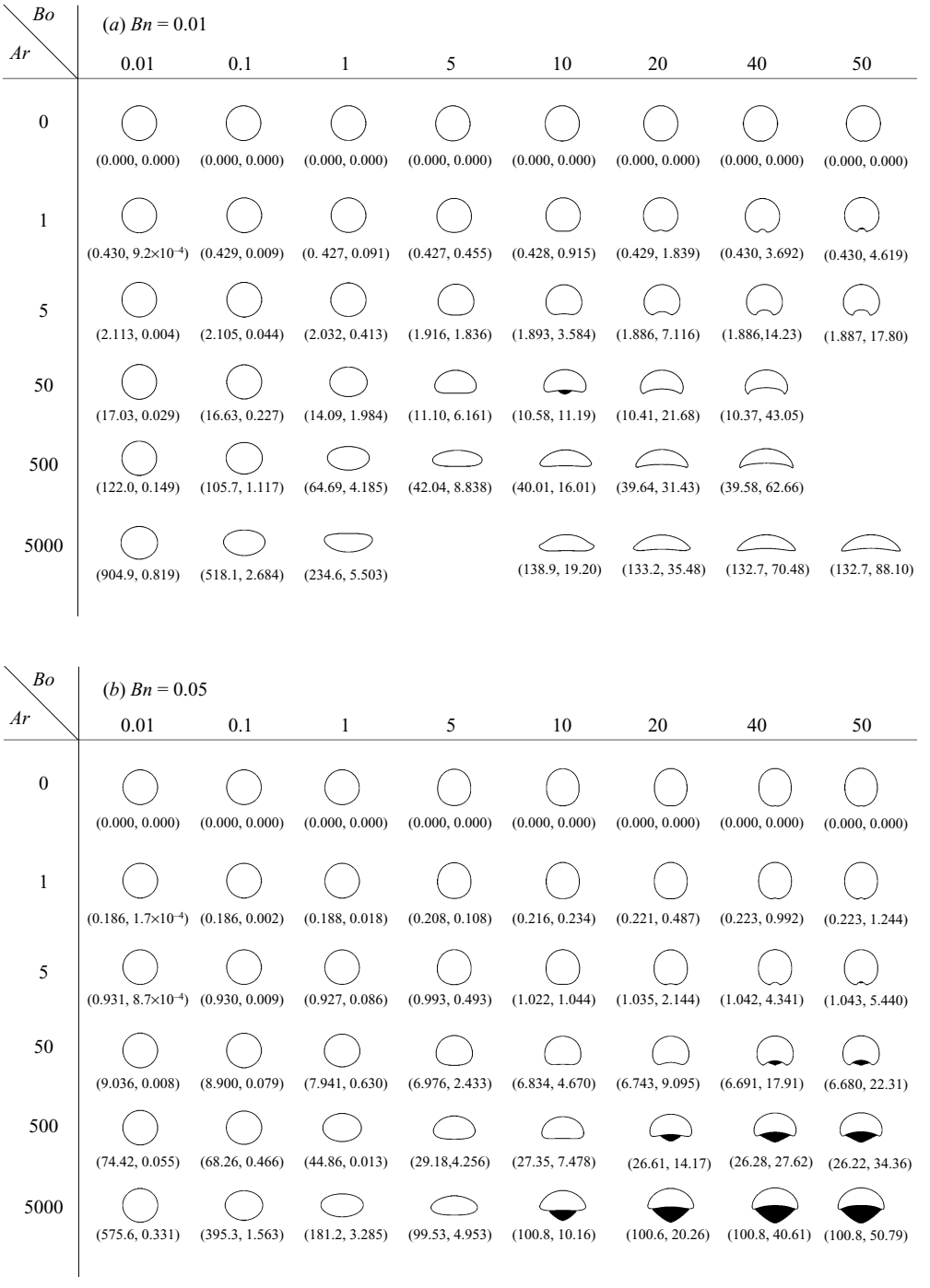

FIGURE 10. For legend see page 145.

yield stress over the capillary forces increase and the bubble has to squeeze through the material. In certain cases in which Newtonian fluid recirculates very slowly at the rear of the bubble, the stress in a viscoplastic fluid is small, with $\|\boldsymbol{\tau}\| \leqslant \tau_y$, and so the

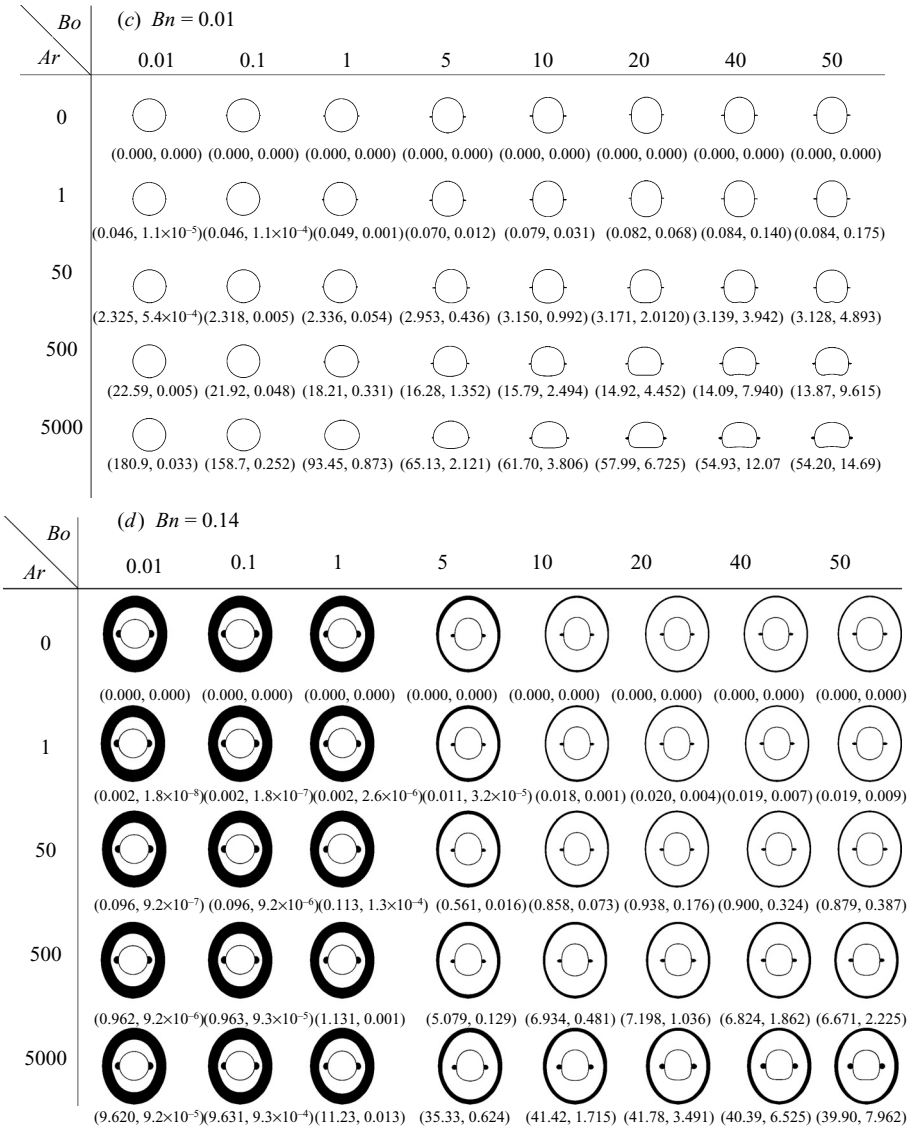

FIGURE 10. For legend see facing page.

material in this region is unyielded. One such case is shown in figure 10(*a*), but such cases populate the entire corner of the shape map with large Bond and Archimedes numbers as *Bn* increases to 0.05 (figure 10*b*) and the effective viscosity increases. Here the unyielded area behind the bubble increases and the bubble deformation from spherical decreases compared to that for a Newtonian fluid. A shape with flatter front side does not arise in the map of bubble shapes with $Bn = 0.05$, in which every location is occupied by a converged solution.

Dubash & Frigaard (2007) have studied experimentally the motion of air bubbles rising under gravity in a column filled with Carbopol solutions. The yield stress of the material they used was $\tau_y^* = 2.2$–2.3 Pa and its other properties and bubble sizes were such that $Bn = 0.0104 - 0.022$, $Ar = 0.466 - 4.31$ and $Bo = 15 - 66$. This range of parameter values is covered in figure 10(*a*, *b*). Unlike our predictions, the bubble

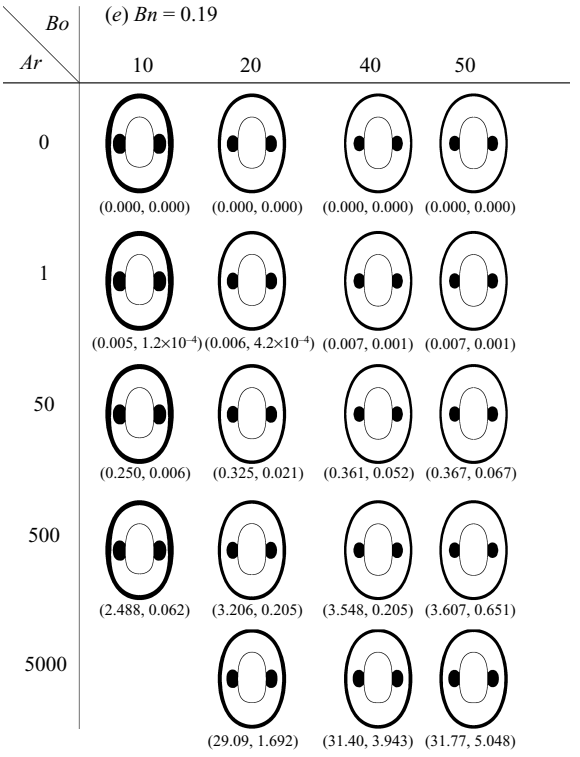

FIGURE 10. Map of bubble shapes in a Bingham fluid as a function of the Bond and Archimedes numbers. Underneath each figure we give the corresponding Reynolds and Weber numbers (Re, We): (a) $Bn = 0.01$, (b) $Bn = 0.05$, (c) $Bn = 0.1$, (d) $Bn = 0.14$ and (e) $Bn = 0.19$. Unyielded material is shown black, and always when it arises in contact with the bubble, but away from the bubble only when it is close enough, $Bn \geqslant 0.14$.

shapes they observed resembled an inverted teardrop. We tried to reproduce these shapes numerically, first using the Papanastasiou model and then using the Herschel–Bulkley model which is more appropriate for the Carbopol solutions used in these experiments, by assuming either shapes closer to the experimental ones as initial bubble shapes to start the Newton–Raphson iterations or higher Bn. Our iterations never converged to such shapes, but to the shapes given in figure 10(a,b). We could attribute the inverted teardrop shape to a number of reasons: (i) Carbopol solutions have a small elasticity which may be important at the rear of the bubble where slower flow takes place and closer to the axis of symmetry the flow is elongational. It is well-known that bubbles assume inverted teardrop shapes in viscoelastic fluids: Astarista & Apuzzo (1965), Pilz & Benn (2007), Malaga & Rallison (2007). (ii) Another reason could be that Carbopol is thixotropic, which could introduce phenomena that cannot be predicted by viscoplastic models, Gueslin *et al.* (2006). (iii) A third reason could be that, in the experiments by Dubash & Frigaard (2007), the bubbles were rising in a tube with diameter not much larger than a typical bubble diameter. In such a narrow tube the fluid must flow downwards closer to the bubble surface giving it a prolate shape. If this deformation is large enough for a liquid drop in creeping flow, Koh & Leal (1989) have shown that the drop shape becomes time-dependent, forming a tail that may constantly elongate and even break. They have also shown that the larger the initial deformation, the smaller the capillary number required for this instability

to arise and that this occurs for a wide range of viscosity ratios between the drop and the host liquid. Presumably this could also take place in a rising bubble and, when the host liquid is viscoplastic, the tail can be 'frozen', so that a stationary shape is obtained. Moreover, Terasaka & Tsuge (2001) have observed that the bubble assumes inverted teardrop shapes when it is formed at a nozzle and this shape is 'frozen' owing to the material's yield stress. Finally, we should mention that experiments with different Carbopol solutions have also been reported by Astarita & Apuzzo (1965) who observed shapes of unconfined bubbles similar to the ones we predict, whereas they observed teardrop shapes in other fluids which were clearly viscoelastic.

As Bn increases to $Bn = 0.1$ (figure 10c), the shape of the bubble has changed in all cases for $Bo \geqslant 0.1$, for reasons that we have mentioned already. For small Bond numbers the bubble remains almost spherical, as surface tension is very important. For $Bo \geqslant 5$ gravitational forces become dominant over surface tension, the effective viscosity around the equatorial plane is higher than that at the poles and the bubble starts to take a bullet-like shape. The bubble retains a flatter rear side than the front side and an indentation for large Bond and Archimedes numbers. As the rate of strain is low enough around the equatorial plane, unyielded material exists there. The sizes of the two unyielded regions, the one far from the bubble and the other around the equatorial plane, increase as Bn increases to 0.14 (figure 10d). For $Bo < 5$ where the bubble is nearly spherical the two unyielded regions are considerably larger than for $Bo \geqslant 5$. At Bn greater than 0.14 and depending on the value of the Bond number, the two regions will start merging, and then the bubble is immobilized and all the material becomes unyielded. For this reason, in figure 10(e), where $Bn = 0.19$, we show cases with $Bo \geqslant 10$ only, so that, although Bn approaches its critical value, the more deformable bubble can take a nearly symmetric prolate shape or a bullet-like shape while rising in the material, irrespective of the values of the other parameters. An envelope of yielded material still completely surrounds the bubble and flow continue to take place. For $Bo < 10$ the flow has stopped and the bubble has been immobilized.

Figure 11 quantifies the bubble shapes by showing their aspect ratio $\chi \equiv h/w$, where h and w are defined in figure 8(a), as a function of Bo for the entire range of Ar we studied and $Bn = 0.01,\ 0.1,\ 0.14$. At the smallest Bn and for $Ar = 1$, the aspect ratio remains very close to unity as Bo increases, since for such materials the bubble remains almost spherical. For larger Ar, the aspect ratio decreases from unity, more so at a larger Ar, until it reaches a plateau, as the bubble assumes an oblate spheroidal shape. In the line with-largest Archimedes number, $Ar = 5000$, and for $4.5 \leqslant Bo \leqslant 9$ there is a discontinuity in the curve of the aspect ratio because stationary bubble shapes could not be calculated there but the bubble shapes changed abruptly there, see figure 10(a). For $Bn = 0.1$ and as Bo increases, the aspect ratio decreases below 1 for $Ar \geqslant 500$ and increases above 1 for $Ar \leqslant 50$ as the bubble assumes a prolate spheroidal shape. For the highest Bn, changes in Ar have a small effect on the aspect ratio as long as $Bo \leqslant 1$. Beyond this Bo value the aspect ratio increases and, above a particular value of Bo which is in the range $10 \leqslant Bo \leqslant 20$, it decreases, more so for the larger Ar, trends which are opposite to those for $Bn = 0.01$. Summarizing, bubbles with small Bn will be either spherical or oblate, but with large Bn they will be either spherical or prolate.

Figure 12 gives the definitions of the width and the height of the unyielded region at the rear side of the bubble and shows that they increase monotonically with the Bond number, the width more so. Such regions arise mainly when $Bn = 0.05$ and they increase with Ar, which generally produces spherical cap shapes, and with Bo, which increases bubble deformability. Given a Bo value, larger inertia produces a flatter

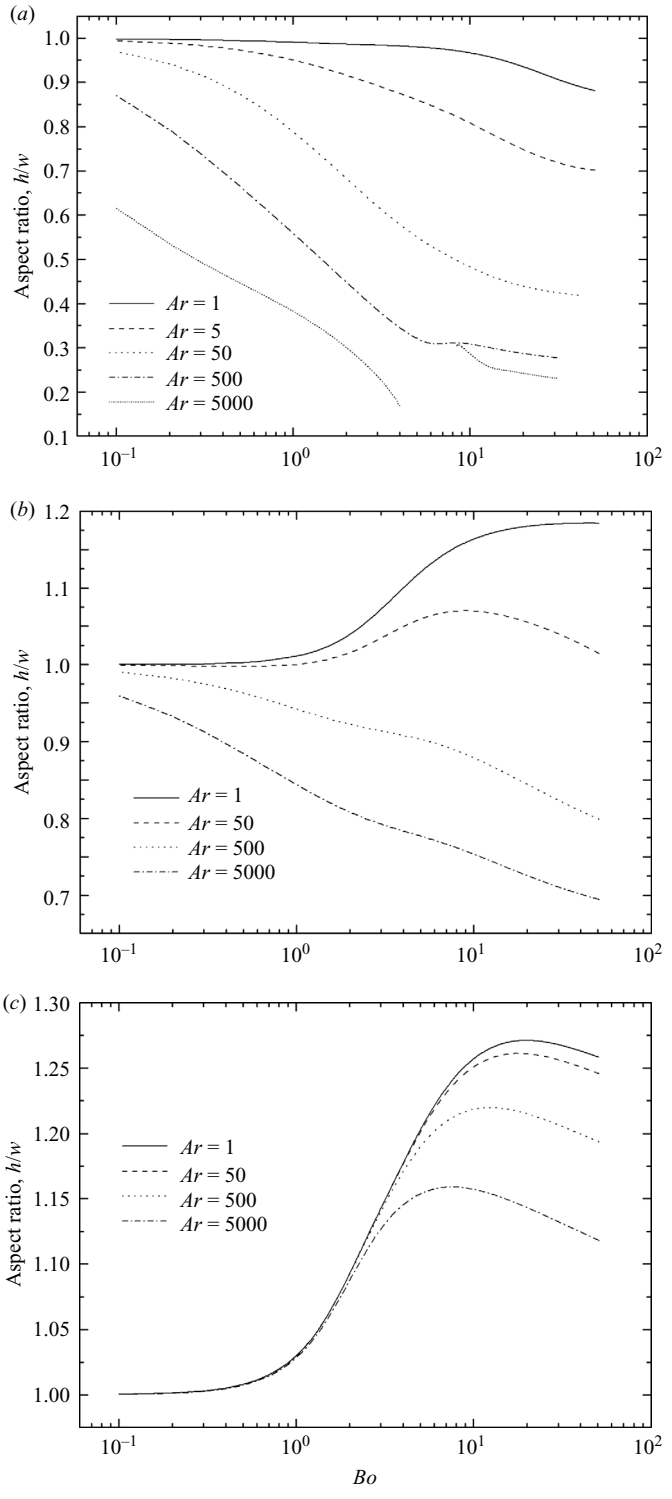

FIGURE 11. Bubble aspect ratio vs. *Bo*, for various *Ar* values and (*a*) $Bn = 0.01$, (*b*) $Bn = 0.1$ and (*c*) $Bn = 0.14$.

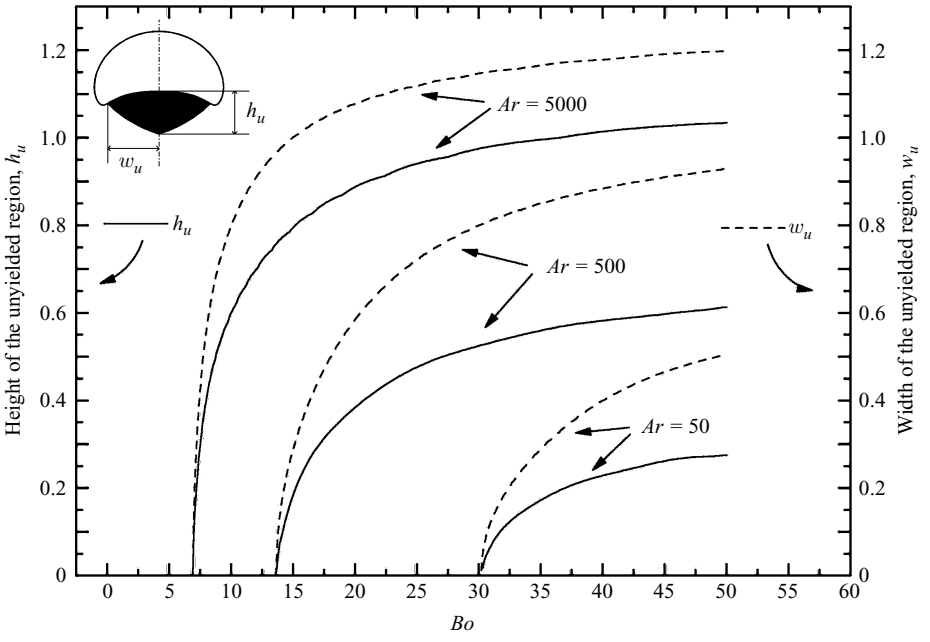

FIGURE 12. Dimensionless width (dashed line) and height (solid line) of the unyielded region behind the bubble vs. Bo, for various Ar values and $Bn = 0.05$. In an inset we show the definitions of these geometric characteristics.

bubble shape which provides a larger shield behind it for unyielded material to exist there. As soon as unyielded material is formed, its size first increases abruptly with Bo, but then both its height and width reach an asymptote which usually do not exceed the radius of the equivalent spherical bubble.

4.3. *Flow field in Bingham fluids*

Figure 13 illustrates the flow field around the bubble in a viscoplastic fluid. Capillary forces are rather weak, $Bo = 30$, while the gravitational forces balance the viscous forces, $Ar = 1$. We show contour plots of radial velocity, on the left half, and azimuthal velocity on the right half of each figure, for low $Bn = 0.01$ (figure 13*a*) and for high $Bn = 0.19$ (figure 13*c*). The total number of equidistant contour lines in this and all other similar plots is 20, unless otherwise mentioned. The outer boundary has been chosen at such a distance that it does not affect the results in any way. For these two cases we have used $R_\infty = 10$, but for clarity in the figures we present a square of side length 10 only. The radial velocity takes its lowest and negative values at the upper side far from the bubble, as the fluid flows downwards, and its highest and positive values at the far lower side of the bubble, while it is zero at the equatorial plane. As mentioned earlier, a boundary condition sets the radial and azimuthal velocities far from the bubble to vary like $\cos(\theta)$ and $\sin(\theta)$, respectively. Our computations show that this dependence remains throughout the unyielded material but not in the yielded material and especially as the bubble surface is approached and Bn increases (see §4.4), indicating that the far-field unyielded material behaves as a solid. The values of the radial velocity are quite large for small Bn, $Bn = 0.01$ (left side of figure 13*a*) where the fluid still behaves similarly to a Newtonian one. As a reminder, the dimensionless far-field ($r \to \infty$) velocity of a spherical bubble in a Newtonian fluid for $Re = 0$ is $U = 1/3$. However, we can see in figure 13(*a*) that even for this small

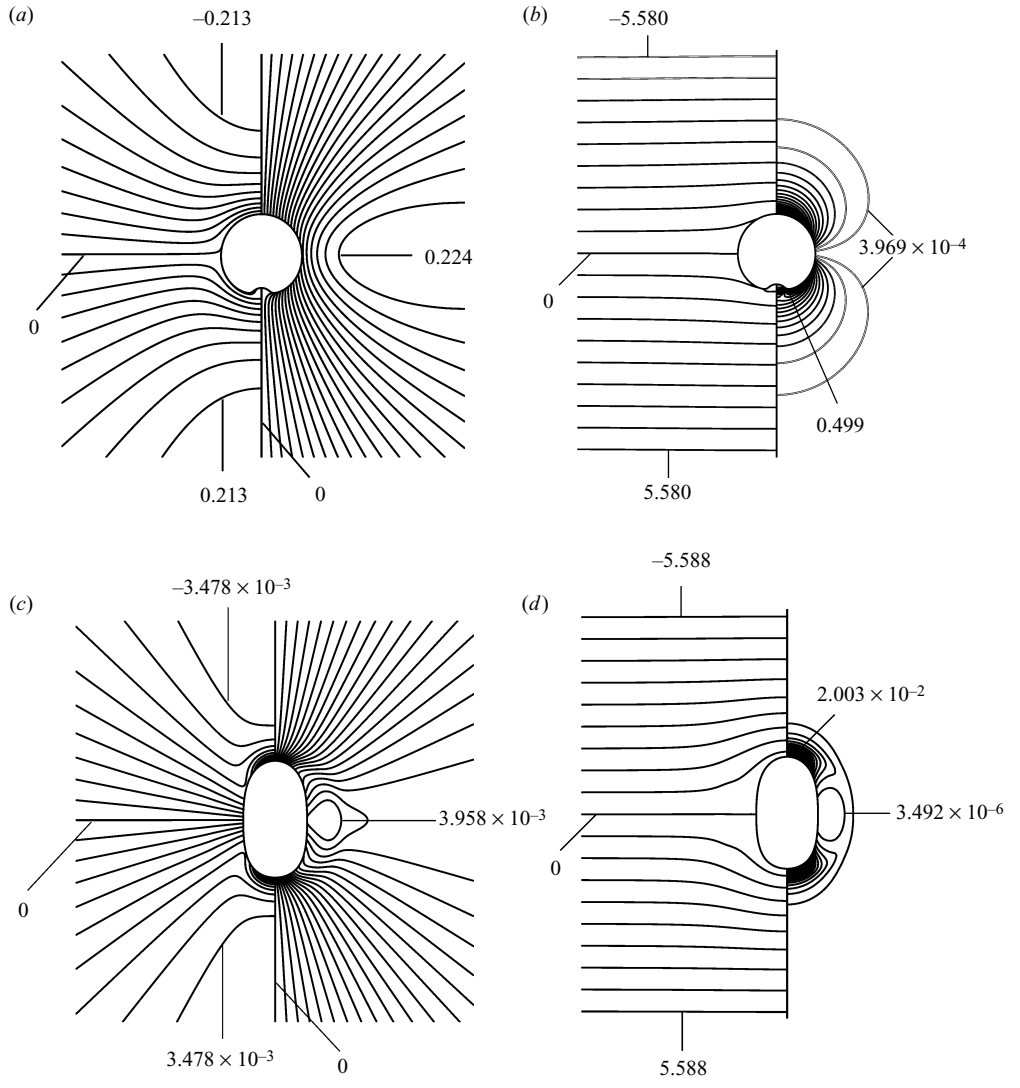

FIGURE 13. (*a*, *c*) Contour plots of the radial, left side, and azimuthal, right side, velocity, and (*b*, *d*) contour plots of the pressure field, left side, and second invariant of the rate of strain tensor, right side, for $Ar = 1$, $Bo = 30$, $R_\infty = 10$, $N = 10^4$ and (*a*, *b*) $Bn = 0.01$ and (*c*, *d*) $Bn = 0.19$. The range of the respective variable is divided into 20 equal intervals.

Bn the far-field ($r = 10$) velocity has decreased to $U = 0.224$. This is a consequence of the viscoplasticity of the fluid and of the shape of the bubble. At higher *Bn*, $Bn = 0.19$, viscoplasticity will further decrease the velocity field around the bubble. Indeed, in figure 13(*c*) the radial velocity is two orders of magnitude smaller, but still varies away from the bubble, following the cosine function. The shape of the bubble is very different in these two cases, as discussed in § 4.2. The azimuthal velocity, for both values of *Bn*, is zero at the axis of symmetry as it should be, while it has its largest values at the equatorial plane. The azimuthal velocity is almost zero inside the indentation that arises at the rear of the bubble for $Bn = 0.01$. Increasing the *Bn* to 0.19, the magnitude of the azimuthal velocity also decreases by 2 orders of magnitude. Here an area of nearly uniform azimuthal velocity arises at the equatorial plane and

in contact with the bubble surface. Indeed, the contour lines of the azimuthal velocity clearly demonstrate that its gradient is much larger at the poles while it decreases to zero at the equatorial plane, where the bubble surface is nearly flat. Figures 13(*b*) and 13(*d*) show the pressure field (left side) and the second invariant of the rate of strain tensor (right side), respectively. For both *Bn* values, the pressure field varies linearly with the axial distance from the bubble, with negative values above it and positive values below it, as expected. The presence of the bubble affects the pressure field only locally and around it. The rate of strain has a local maximum at the poles, a local minimum around the equatorial plane near the bubble and tends to zero at infinity. Calculating $\dot{\gamma}$ for a spherical bubble moving in a Newtonian fluid, where the analytical solution is known, we find that at $(\theta = \pi/2,\ r = 1)$, $\dot{\gamma} = 0$, whereas $\dot{\gamma} \neq 0$ at $\theta = 0$ and $\theta = \pi$. The existence of even one point on the bubble surface where $\dot{\gamma} = 0$ forces the material to become unyielded there; this slows down the flow field and decreases $\dot{\gamma}$ around it. This eventually leads to the creation of a finite domain in the material that is unyielded. In figure 13(*b*), we observe that $\dot{\gamma}$ has a local maximum at the bubble tip at the rear of the bubble and abruptly decreases as we move towards the south pole of the bubble. However, it does not become small enough to allow unyielded material to form inside the small indentation which exists there. This occurs for other parameter values as seen in figures 10(*a*, *b*). On the contrary, in figure 13(*d*), the larger *Bn* reduces the values that $\dot{\gamma}$ takes and gives the bubble a prolate shape without a tip or an indentation. Hence, $\dot{\gamma}$ varies smoothly around the bubble surface and is symmetric with respect to the equatorial plane of the bubble. For both values of *Bn* the values of $\dot{\gamma}$ where unyielded material exists are smaller by over three orders of magnitude than those in the rest of the material.

In figure 14, we show corresponding contours for the same four variables and the same *Bo*, but larger buoyancy with respect to dynamic viscosity, $Ar = 50$. For $Bn = 0.01$ (figure 14*a*, *b*), the bubble has the shape of a spherical cap with a tip in its rear side. For $Bn = 0.19$ (figure 14*c*, *d*), the bubble takes a prolate shape and is nearly flat at its equatorial plane. In the smaller *Bn* case, the radial velocity is larger, but quite asymmetric before and after the bubble because of the large vortex that is formed in the bubble wake. The pressure contours remain straight and horizontal away from the bubble and are slightly affected by it and only in its vicinity. The rate of strain has a local sharp maximum at the bubble tip and becomes very low in its wake, but unyielded material does not arise there. On the contrary, for $Bn = 0.19$, the velocity components are much smaller, have a plane of symmetry and the azimuthal velocity is very small at the equatorial plane near the bubble. At this same location, the rate of strain takes its lowest values (smaller by 4 orders of magnitude than its maximum at the poles) giving rise to unyielded material in contact with the bubble.

Selected cases of bubble shapes and streamlines are shown in figure 15. The particular values of the stream function are given in each figure. For the lowest Bingham number we examined, $Bn = 0.01$, the streamlines do not deviate appreciably from the corresponding ones for a Newtonian fluid and no unyielded material arises in contact with the bubble. In particular, for $Ar = 1,\ Bo = 50$ (figure 15*a*) an indentation is formed behind the bubble and the streamfunction assumes very small and negative values in this region, indicating flow separation. As the Archimedes number increases to 500 (figure 15*b*), a vortex is formed behind the bubble, which takes an oblate shape with rounded edge for $Bo = 10$ or more pointed edge at higher Bond numbers, $Bo = 40$ (figure 15*c*). At even higher Bond numbers it is possible that skirted bubbles could be formed in analogy to those in Newtonian fluids. Figure 15(*d*) shows a particular bubble shape that arises for $Ar = 5000$ and $Bo = 4.5$ just before the region in which

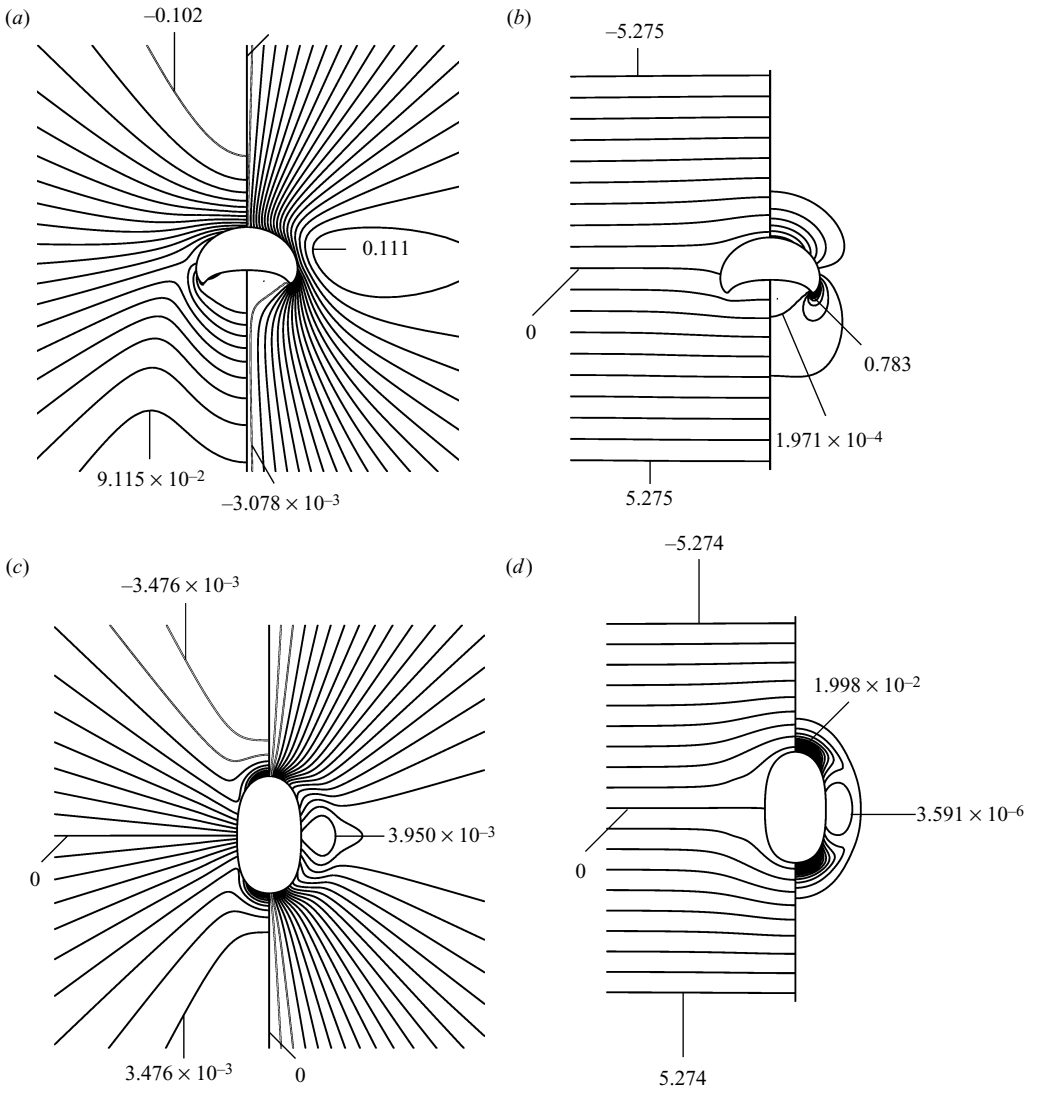

FIGURE 14. As figure 13 but for $Ar = 50$.

steady bubble shapes could not be computed for this Bingham number or for a Newtonian fluid; see figures 5 and 10*a*. Here the bubble edge is smooth but tilted in the upstream direction, the bubble resembles a hat and the vortex behind it is fairly large. A slight increase of the Bingham number to 0.05 eliminates flow separation and the vortex behind the bubble, see figure 15(*e*), which is a common feature in general for $Bn \geqslant 0.05$. Increasing the Bingham number further to 0.1 (figure 15*f*) or 0.14 (figure 15*g*) produces more rounded bubbles with a prolate shape and, hence, streamlines that are less curved around the bubble.

We have measured and depict in figure 16 the size and the location of the vortex behind the bubble in a Bingham fluid only for $Bn = 0.01$. These geometric characteristics were defined in figure 8(*a*). Figure 16(*a*) clearly shows that the vortex length and width increases with both the Archimedes and the Bond numbers. Similarly

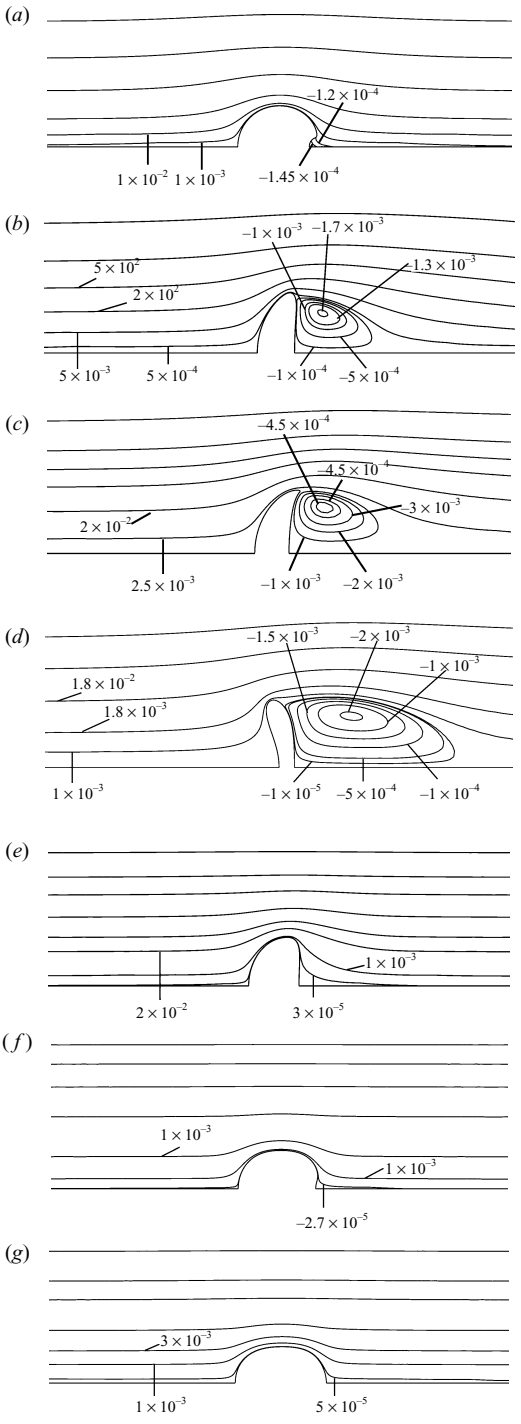

FIGURE 15. Bubble shapes and streamlines for (*a*) $Ar=1$, $Bo=50$, $Bn=0.01$, (*b*) $Ar=500$, $Bo=10$, $Bn=0.01$, (*c*) $Ar=500$, $Bo=40$, $Bn=0.01$, (*d*) $Ar=5000$, $Bo=4.5$, $Bn=0.01$, (*e*) $Ar=500$, $Bo=10$, $Bn=0.05$, (*f*) $Ar=50$, $Bo=50$, $Bn=0.1$, (*g*) $Ar=50$, $Bo=20$, $Bn=0.14$.

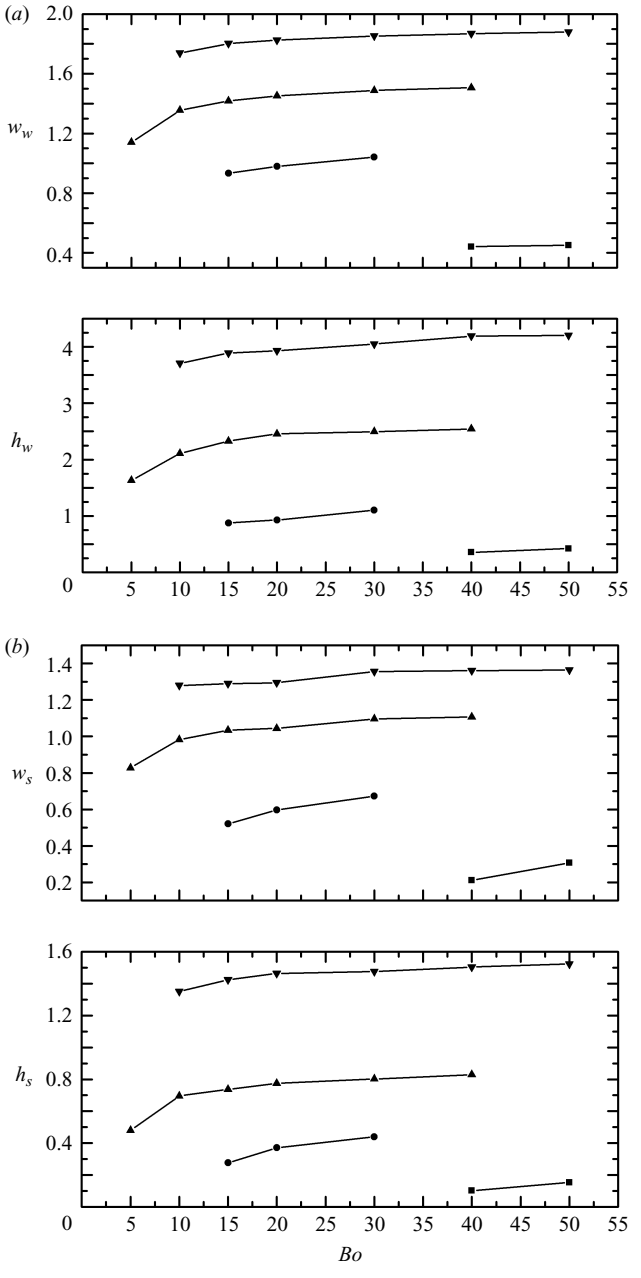

FIGURE 16. (*a*) Length and width of the vortex behind the bubble and (*b*) distance of its centre from the bubble centre and the axis of symmetry for $Bn = 0.01$. (■, $Ar = 5$; ●, $Ar = 50$; ▲, $Ar = 500$; ▼, $Ar = 5000$).

figure 16(*b*), shows that its centre becomes further away from the bubble back side and the axis of symmetry as these dimensionless parameters increase.

4.4. *Dynamic parameters of flow and critical Bingham number for bubble entrapment*

The magnitude of the bubble rise velocities or equivalently the magnitude of the far-field velocities in a frame moving with the bubble is given in terms of the

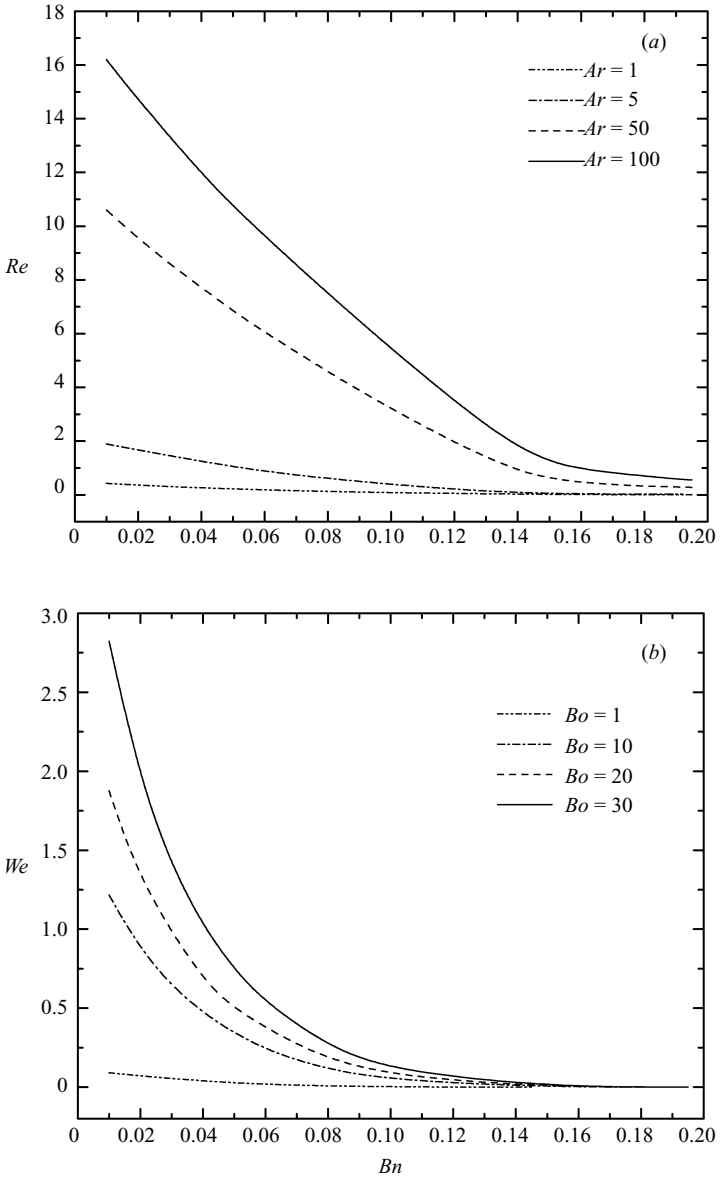

FIGURE 17. Dependence of (*a*) *Re* on *Bn* for $Bo = 10$ and (*b*) *We* on *Bn* for $Ar = 1$.

corresponding Reynolds or Weber number as a function of the Bingham number in figure 17. Both these dynamic parameters are post-calculated based on the bubble velocity according to (4.2) and (4.3). The Bond number is fixed in figure 17(*a*) at $Bo = 10$. As *Ar* increases, *Re* increases as well, more so for small Bingham numbers. Moreover, as *Bn* increases *Re* decreases because the bubble rise velocity decreases and at a critical *Bn* the bubble stops moving, irrespective of the value of *Ar* and *Bo* because all the material becomes unyielded. The dependence of *We* on *Bn* is similar to that of *Re*, as shown in figure 17(*b*), for $Ar = 1$ and for different values of *Bo*. The Weber number increases monotonically with *Bo* and decreases with *Bn*. Apparently, lines of different *Bo* approach zero for different values of *Bn*, indicating that capillary

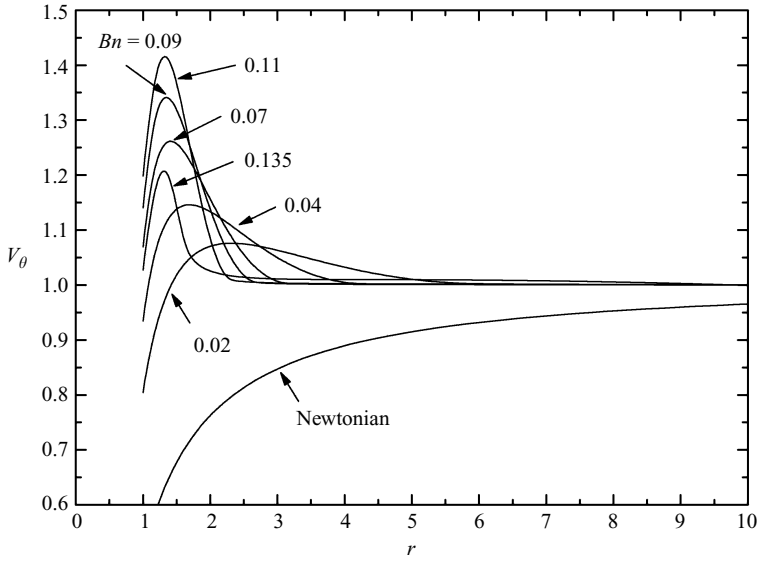

FIGURE 18. Radial profiles of the azimuthal velocity at $\theta = \pi/2$ for different values of Bn and $Re = 0.04$, $Bo = 0.01$.

forces will affect the critical level of yield stress in a material that will cause bubble entrapment. The exact condition for bubble entrapment is not easy to determine from this figure or from plotting the drag force on the bubble as a function of Bn, because Papanastasiou's constitutive equation does not discriminate between yielded and unyielded domains *a priori* and allows some residual flow even where unyielded material is found *a posteriori*. So a clear asymptote in the drag force, like the one produced in figure 6 of BTAB, should not be expected.

A first possible determining the conditions for bubble entrapment in a viscoplastic fluid is to perform a plastic boundary layer analysis assuming that the bubble remains spherical, i.e. the Bond and Archimedes numbers are fairly small, parallel to the analysis in BTAB for a solid sphere. Under this assumption, we first examined whether a boundary layer is formed around a bubble and whether the Papanastasiou model can capture it by plotting the radial profile of the azimuthal velocity at the bubble equatorial plane with Bn as a parameter. Unlike the analysis in BTAB, here the bubble rise velocity is determined as part of the solution and decreases with Bn, whereas on the bubble surface it is not zero, owing to the zero-shear boundary condition applied there. In order to compare the various profiles with each other more easily, we normalized the azimuthal velocity so that it is equal to 1 away from the bubble. The computed profiles are shown in figure 18, where we have kept the same low value for the Reynolds number, $Re = 0.04$, in analogy with the creeping flow conditions in BTAB. We observe that the azimuthal velocity for a Newtonian fluid approaches its far-field value monotonically. On the contrary, in a Bingham fluid it exhibits a maximum, which moves closer to the bubble and becomes sharper as the Bingham number increases. This occurs because the outer yield surface moves closer to the bubble decreasing the width of the path through which material can still flow through the equatorial plane. This approach of the velocity maximum to the bubble surface indicates the formation of a boundary layer. At $r = 1$, the location of the bubble surface at the equatorial plane, the azimuthal velocity is not zero as

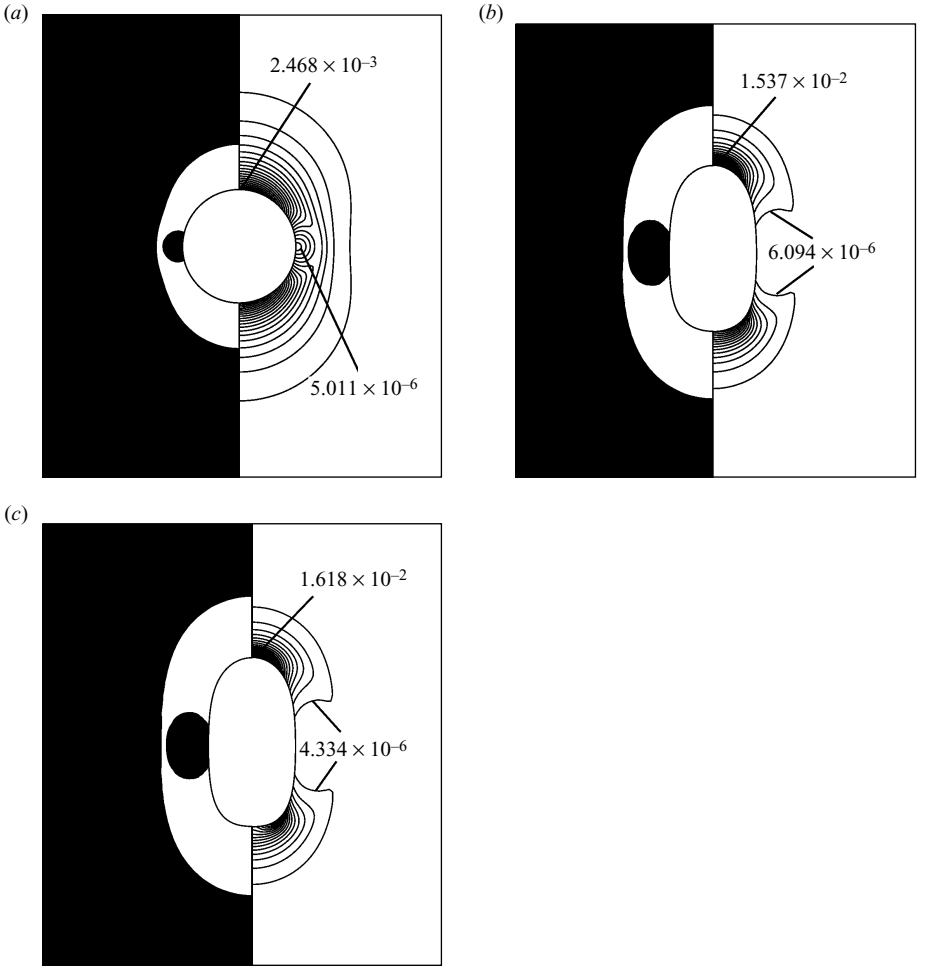

FIGURE 19. Yielded (white) and unyielded (grey) domains, left half, and contour plots of the second invariant of the rate of strain, right half, near the critical Bingham number for $N = 10^4$, $R_\infty = 10$, and (*a*) $Bn = 0.142$, $Ar = 1$, $Bo = 0.1$, (*b*) $Bn = 0.198$, $Ar = 50$, $Bo = 15$, and (*c*) $Bn = 0.201$, $Ar = 5000$, $Bo = 30$.

in the case of a solid sphere (see figure 10 in BTAB), but equals the bubble surface velocity there because of the zero-shear condition. As Bn increases, this velocity first increases above its far-field value, $0.04 \leqslant Bn \leqslant 0.11$, but then it decreases towards it as critical conditions are approached and the two yield surfaces tend to merge, $Bn = 0.135$. Unfortunately, the inevitable formation of unyielded material around the bubble equator, the shape and size of which depends on Bn, makes the necessary scaling arguments very complicated and the outcome of this semi-analytical approach questionable.

Instead, it is reasonable to consider that the bubble motion stops and that Bn has reached its critical value when the unyielded area away from the bubble merges with the one around its equatorial plane. Such a situation just before the two yield surfaces merge is shown in figure 19 for three different sets of material parameters. If the third decimal place of Bn increases by even one unit in each of the three cases the two yield surfaces will merge. On the left half of each figure we show the bubble and the yielded

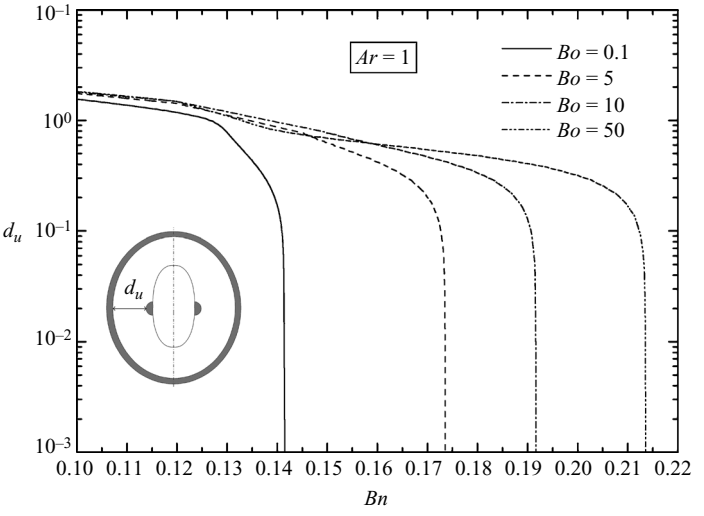

FIGURE 20. Variation of the distance between the two yield surfaces at the equatorial plane, d_u vs. Bn for various Bo. In an insert we show the definition of this distance.

domains in white and the unyielded domains in grey, while on the right half of each figure we show the second invariant of the rate of strain tensor. In all cases, we see that although the two unyielded regions are about to merge, $\dot{\gamma}$ is nowhere equal to zero, but where unyielded material is predicted it takes values that are smaller by 3–4 orders of magnitude than in the rest of the material and certainly below the critical value N^{-1} for the Papanastasiou model as explained in § 3.3. So even when the two regions have merged, finite motion of the material is predicted, albeit with very large viscosity and, hence, very small velocity. Figure 19 also demonstrates that the critical Bn at which the bubble will stop moving is distinct for the three cases and depends mostly on the shape of the bubble. The higher the Bond number is, the more the bubble is deformed, becoming elongated in order to squeeze through the material as the critical condition approaches. This concurs with the conclusion of Dubash & Frigaard (2007) who, based on scaling arguments, mentioned that larger and more deformable bubbles are more difficult to immobilize. The variation of the distance between these two surfaces at the equatorial plane, d_u, is shown in figure 20. It decreases slowly with Bn up to a critical point, after which it decreases exponentially and meets the x-axis at increasing values of Bn as Bo increases. We call the point of intersection with the x-axis the critical Bingham number, Bn_c. Its values, shown in figure 21, are independent of the Archimedes number, when $Ar < 100$, and only slightly dependent on it at higher Ar values. The Bond number does not affect Bn_c, if it is so small that surface tension does not allow the bubble to deform from its spherical shape, i.e. $Bo \leqslant 0.1$, or so large that bubble deformation is restricted by the outer yield surface, the shape of which does not vary much with the surface tension of the bubble, i.e. $Bo \geqslant 50$. In these calculations of the critical conditions we used a mesh of the type given in figure 2(b) with $N = 10^4$. We repeated this calculation with a mesh of the type given in figure 2(c) with an even larger value $N = 5 \times 10^4$. The results are given in table 5 and demonstrate that neither the value of N nor the structure and density of the mesh affect them. It is noteworthy that the Bingham number used so far in this work is related to the so-called yield stress parameter, Y_g,

Mesh, N/Bo	0.1	5	10	50
M1, 10^4	0.143	0.175	0.192	0.212
M2, 5×10^4	0.142	0.174	0.192	0.214

TABLE 5. Critical Bn values as a function of Bo for two meshes (figures 2a and 2c) and values of N 10^4 and 5×10^4 at $Ar = 1$.

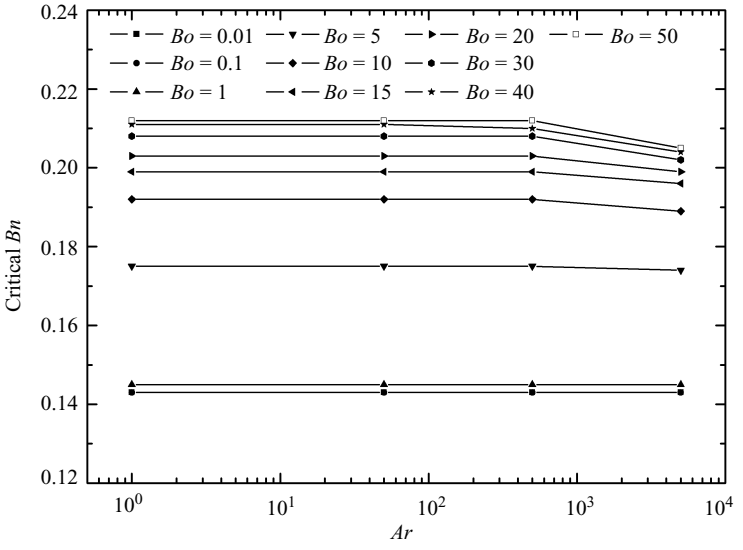

FIGURE 21. Dependence of critical Bingham number on Bond and Archimedes numbers. The curves with $Bo = 0.01$ and 0.1 are indistinguishable.

of BTAB by

$$Y_g = \tfrac{3}{2} Bn. \tag{4.6}$$

The critical value for entrapment of a sphere in a Bingham fluid under creeping flow conditions was found in BTAB to be $Y_g = 0.143$, i.e. it is smaller by a factor of 2/3 than that for a non-deformable bubble under the same conditions. This is the same ratio as the ratio of the terminal velocity of a solid sphere to that of a spherical bubble under the same buoyancy force. Clearly, the more retarding no-slip condition on the solid sphere requires a smaller yield stress to entrap it in a Bingham fluid than the shear free condition on a bubble surface.

As the two yield surfaces tend to merge, the magnitudes of the velocity and rate of strain fields decrease everywhere in the domain that is still yielded. We stopped our computations at the value of Bn for which they have just merged, because beyond that value the numerical error in computing such small variables becomes significant. In any case, it reasonable to monitor the bubble rise velocity as the Bingham number increases. This is shown in figure 22, for just the first case given in figure 20, where $Ar = 1$ and $Bo = 0.1$. We observe that as the Bingham number increases the logarithm of the terminal velocity decreases, but for $Bn > 0.13$ the slope of the curve decreases abruptly and then increases again. We attribute the sharp decrease in the slope to the approach of critical conditions, but the subsequent increase to the numerical error we described above. We have taken the slope of this curve at its inflection point and we can clearly see that it intersects the abscissa at $Bn \approx 0.142$. In other words,

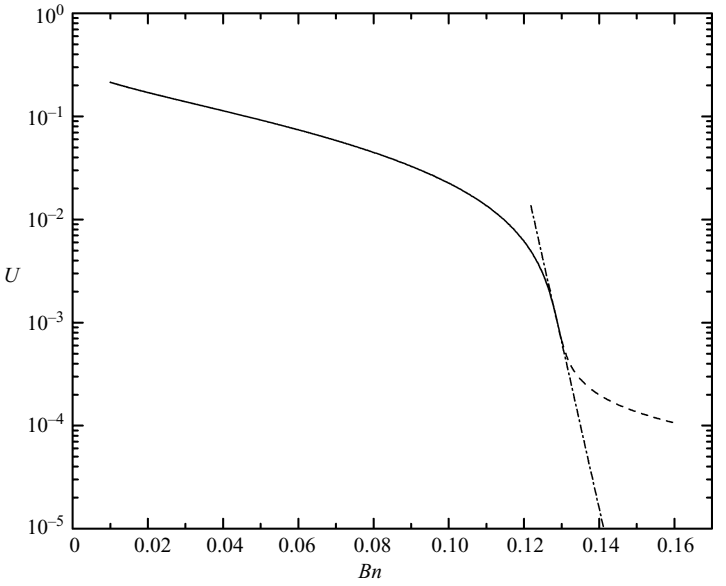

FIGURE 22. Dimensionless bubble rise velocity vs. Bn for $Ar = 1$ and $Bo = 0.1$.

monitoring the terminal velocity results in the same critical Bingham number. The outcome similar is for all other cases we examined. This abrupt change in slope corresponds to the abrupt change in slope of the terminal velocity vs. bubble volume experimentally measured by Astarista & Apuzzo (1965). Unfortunately, these authors did not report the value of the material's yield stress, so we cannot convert their bubble volumes to our Bingham numbers and directly compare our predictions to their measurements.

Dubash & Frigaard (2007) experimentally determined the critical Bingham number for bubble rise in a Bingham fluid and found that, depending on bubble aspect ratio, it varied between 0.01 and 0.15. Their upper limit falls within our predictions, although it should be recalled that the experimental bubble shapes resembled inverted teardrops and this should affect their mobility. On the contrary, the prediction of Bn_c, using variational principles and a Newtonian flow field around a spherical bubble by the same authors (Dubash & Frigaard 2004) grossly overestimates it, since it places it in the range of 0.7–2. We examined the predictions of two inequalities resulting from these variational principles (Theorem 3) using the flow field and the bubble shape we have predicted in this work. Starting with very small Bn values the predicted Bn_c values are about 0.7, as reported by Dubash & Frigaard (2004). Increasing the Bn of the material affects not only the bubble shape but also the flow field qualitatively as mentioned previously. This results in a continued decrease of the Bn_c value up to $Bn \approx 0.12$, for which $Bn_c \approx 0.25$. However, for larger values of Bn, Bn_c started to increase. This is probably caused by the very small values of $\dot{\gamma}$ that arise in the denominator of the inequality (35) in Dubash & Frigaard (2004). The situation did not change when inequality (51) was used.

Figure 23 shows the dependence of the bubble velocity (in mm s^{-1}) on the equivalent bubble radius (in mm) with the material's yield stress as a parameter, keeping the other material properties close to those reported by Maxworthy *et al.* (1996) for the mixture of 80 % glycerin in water. For small bubbles, their rise velocity is zero

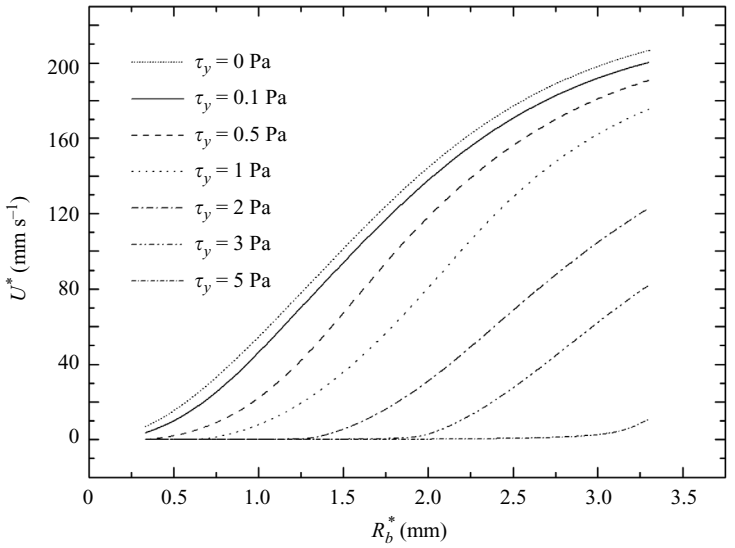

FIGURE 23. Dimensional bubble rise velocity vs. dimensional bubble radius for various viscoplastic fluids with surface tension, $\gamma^* = 0.0655\,\mathrm{N\,m^{-1}}$, density, $\rho^* = 1008\,\mathrm{kg\,m^{-3}}$, and viscosity, $\mu_o^* = 0.0601\,\mathrm{N\,s\,m^{-2}}$.

irrespective of the yield stress, but it smoothly increases as the bubble size increases. This is understandable, given that an increase in bubble radius decreases *Bn*. Bubble mobilization occurs earlier and higher velocities are attained for materials with a smaller yield stress. For easier comparison we have also included in the same figure the bubble terminal velocity in a Newtonian fluid. Finally the drag coefficient is shown as a function of the Bingham number for a given value of *Ar* (figure 24*a*) or for a given value of *Bo* (figure 24*b*). In all cases, increasing *Bn* from zero increases C_d by several orders of magnitude and more abruptly as the critical conditions are approached, and for all practical cases the bubble is immobilized. The values of C_d and its increase are larger for a less deformable bubble ($Bo = 0.01$) with less inertia ($Ar = 1$). As expected, given a value of *Ar*, increasing *Bo* decreases the drag coefficient as the bubble deformability increases. Furthermore, given a value of *Bo*, increasing *Ar* decreases the drag coefficient. This should be expected also, since according to (4.4) C_d is inversely proportional to *Ar*. The same dependence is observed for a Newtonian fluid with $Bn = 0$, which concurs with the fact that here C_d is inversely proportional to *Re*. However, instead of approaching a vertical asymptote, as in the case of a solid sphere (see BTAB), at some value of *Bn*, all curves attain a smaller slope. In the single case of a non-deformable bubble this is attributed to numerical error at these extreme values of $C_d \approx 10^8$, while in all other cases the change of slope is associated with a change in the shape of a deformable bubble. Indeed, in figure 25 we plot the bubble height, *h*, and the axial distance of the outer yielded surface at the axis of symmetry, S_u, as a function of the Bingham number. We observe that for small values of *Bn*, *h* does not change for $Bo = 0.1$ and slightly increases for $5 \leqslant Bo \leqslant 50$, whereas S_u decreases as the outer yield surface approaches the bubble, more so at the axis of symmetry; see figure 9(*a*). Above a characteristic value of *Bn*, *h* increases significantly and almost linearly, whereas S_u either decreases with a larger slope and tends to intersect the *h* curve ($Bo = 0.1$), decreases with a smaller slope ($Bo = 5$) or increases for the remaining Bond numbers. In other words, at these characteristic *Bn* values

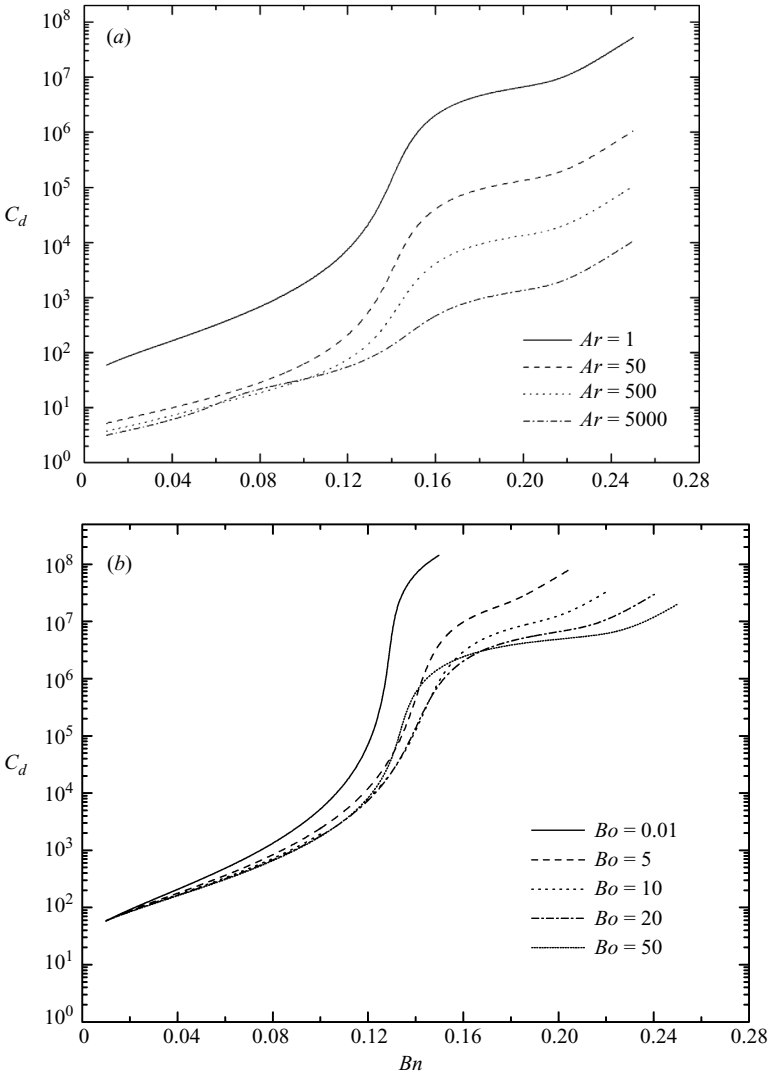

FIGURE 24. The drag coefficient as a function of the Bingham number, for various values of (*a*) *Ar* and (*b*) *Bo*.

either (i) the outer yield surface approaches the bubble surface very rapidly and the bubble is entrapped ($Bo = 0.1$), or (ii) the bubble elongates forcing the outer yield surface to decrease its rate of approach to it, delaying bubble entrapment to higher *Bn* values ($Bo = 5,\ 10$), or (iii) the bubble is slightly squeezed by the approaching yield surface and then elongates as in (ii) ($Bo = 50$). The values of *Bn* at which the bubble starts to elongate correspond to the inflection points in the drag force in figure 24(*b*).

5. Conclusions

We simulated the rise of a bubble in a viscoplastic material for a wide range of material parameters. The simulation is based on the mixed finite element method for the discretization of the governing equations coupled with a quasi-elliptic mesh generation scheme in order to follow the large deformations of the physical domain.

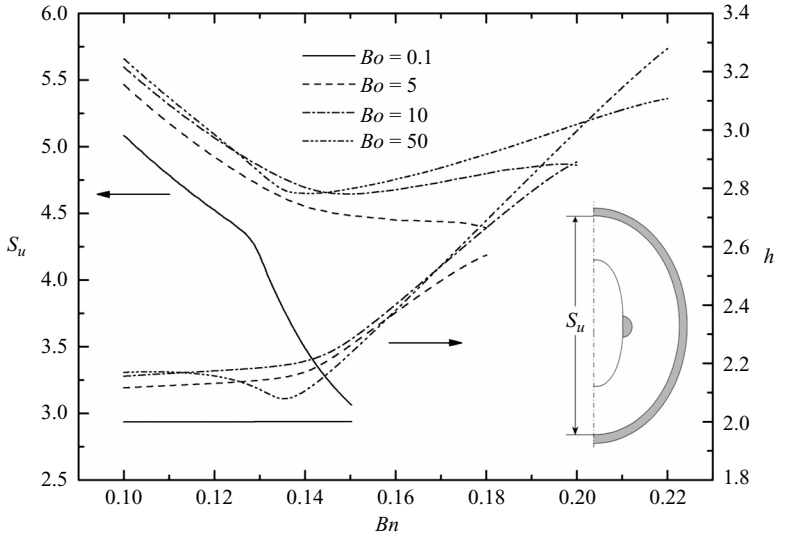

FIGURE 25. Bubble height, h, and axial distance of the outer yield surfaces, S_u, at the axis of symmetry vs. Bn.

Our results allow us to determine the evolution of (a) the velocity and pressure fields in the fluid, (b) the shape of the liquid/air interface, (c) the domain of the unyielded material, (d) the critical Bingham number for bubble entrapment and (e) the dynamic parameters of the flow including the drag coefficient.

We examined the effect of the yield stress and the capillary, viscous and gravity forces. First, we verified the accuracy of our new code by comparing our results with previous theoretical and experimental ones for a Newtonian fluid. Where possible, we extended earlier results to larger values of Reynolds and Weber numbers. In a viscoplastic fluid, the bubble rise velocity and, hence, both the Reynolds and Weber numbers decrease as the yield stress increases. Unyielded material exists at the rear of the bubble at low Bingham numbers and large Bond and Archimedes numbers, when the bubble has a distorted oblate spheroidal shape. This unyielded area disappears at higher Bingham numbers as the shape of the bubble changes to a bullet-like shape allowing it to squeeze through the material. Unyielded material also arises around and far from the bubble and around the equatorial plane for $Bn \geqslant 0.1$. The size of these domains increases with the Bingham number and when they merge the bubble stops moving. As this critical Bingham number is approached the bubble tends to take a bullet-like shape owing to the higher effective viscosity at its equatorial plane and the lower viscosity at its poles. The critical Bingham number has strong dependence on the Bond number, an increase of which allows the bubble to deform more. Finally the drag coefficient decreases with the Bond and Archimedes numbers and increases with the Bingham number.

The predicted bubble shapes and the drag coefficient can be used to determine the material parameters, μ_o^* and τ_y^*. The numerical approach presented here can be extended to calculate mass transfer coefficients from/to a bubble in a yield-stress fluid, which are unavailable today, despite being extremely important in determining optimal operating conditions for various chemical and physical processes.

We thank the European Social Fund (ESF) and the Operational Program for Educational and Vocational Training II (EPEAEK II) and particularly the Pythagoras II program for funding the above work. N.C. acknowledges the financial support of the PENED 2001 research program of the GSRT of Greece. We appreciate very much the very constructive comments made by the referees.

REFERENCES

Astarista, G. & Apuzzo, G. 1965 Motion of gas bubbles in non–Newtonian liquids. *AIChE J.* **11**, 815–820.

Bercovier, M. & Engelman, M. 1980 A finite element method for the incompressible non-Newtonian flows. *J. Comput. Phys.* **36**, 313–326.

Beris, A. N., Tsamopoulos, J. A., Armstrong, R. C. & Brown, R. A. 1985 Creeping motion of a sphere through a Bingham plastic. *J. Fluid Mech.* **158**, 219–244.

Bhaga, D. & Weber, M. E. 1981 Bubbles in viscous liquids: shapes, wakes and velocities. *J. Fluid Mech.* **105**, 61–85.

Bingham, E. C. 1922 *Fluidity and Plasticity*. McGraw-Hill.

Blackery, J. & Mitsoulis E. 1997 Creeping motion of a sphere in tubes filled with a Bingham plastic material. *J. Non-Newtonian Fluid Mech.* **70**, 59–77.

Blanco, A. & Magnaudet, J. 1995 The structure of the axisymmetric high-Reynolds number flow around an ellipsoidal bubble of fixed shape. *Phys. Fluids* **7**, 1265–1274.

Bonometti, T. & Magnaudet, J. 2006 Transition from spherical cap to toroidal bubbles. *Phys. Fluids* **18**, 052102 1–12.

Bonometti, T. & Magnaudet J. 2007 An interface capturing method for incompressible two phase flows validation and application to bubble dynamics. *Intl. J. Multiphase Flow* **33**, 109–133.

Burgos, G. R., Alexandrou, A. N. & Entov, N. M. 1999 On the determination of yield surfaces in Herschel-Bulkley fluids. *J. Rheol.* **43**, 463–483.

Christov, C. I. & Volkov, P. K. 1985 Numerical investigation of the steady viscous flow past a stationary deformable bubble. *J. Fluid Mech.* **158**, 341–364.

Clift, R., Grace, J. R. & Weber, M. E. 1978 *Bubbles, Drops and Particles*. Academic.

Dimakopoulos, Y. & Tsamopoulos, J. 2003*a* Transient displacement of a viscoplastic material by air in straight and suddenly constricted tubes. *J. Non-Newtonian Fluid Mech.* **112**, 43–75.

Dimakopoulos, Y. & Tsamopoulos, J. 2003*b* A quasi-elliptic transformation for moving boundary problems with large anisotropic deformations. *J. Comput. Phys.* **192**, 494–522.

Dimakopoulos, Y. & Tsamopoulos, J. 2003*c* Transient displacement of a Newtonian fluid by air in straight or suddenly constricted tubes. *Phys. Fluids* **15**, 1973–1991.

Dimakopoulos, Y. & Tsamopoulos, J. 2004 On the gas-penetration in straight tubes completely filled with a viscoelastic fluid. *J. Non-Newtonian Fluid Mech.* **117**, 117–139.

Dimakopoulos, Y. & Tsamopoulos, J. 2006 Transient displacement of Newtonian and viscoplastic liquid by air in complex tubes. *J. Non-Newtonian Fluid Mech.* doi:10.1016/j.jnnfm.2006.08.002.

Dubash, N. & Frigaard, I. 2004 Conditions for static bubbles in viscoplastic fluids. *Phys. Fluids* **16**, 4319–4330.

Dubash, N. & Frigaard, I. 2007 Propagation and stopping of air bubbles in Carbopol solutions. *J. Non-Newtonian Fluid Mech.* **142**, 123–134.

Duineveld, P. 1995 The rise velocity and shape of bubbles in pure water at high Reynolds number. *J. Fluid Mech.* **292**, 325–332.

Foteinopoulou, K., Mavrantzas, V., Dimakopoulos, Y. & Tsamopoulos, J. 2006 Numerical simulation of multiple bubbles growing in a Newtonian liquid filament undergoing stretching. *Phys. Fluids* **18**, 042106.

Frigaard, I. & Nouar, C. 2005 On the usage of viscosity regularization methods for visco-plastic fluid flow computation. *J. Non-Newtonian Fluid Mech.* **127**, 1–26.

Glowinski, R., Lions, J. & Trémolières, R. 1981 *Numerical Analysis of Variational Inequalities*, North-Holland.

Gueslin, B., Talini, L., Herzhaft, B., Peysson, Y. & Allain, C. 2006 Flow induced by a sphere settling in an aging yield-stress fluid. *Phys. Fluids* **18**, 103101.

HABERMAN, W. L. & MORTON, R. K. 1953 An experimental investigation of the drag and shape of air bubbles rising in various liquids. Report 802, Navy Dept., David W. Taylor Model Basin. 68 Washington, DC.

HADAMARD, J. S. 1911 Mouvement permanent lent d'une sphère liquide et visqueuse dans un liquide visqueux. *C. R. l'Acad. Sci. Paris* **152**, 1735–1738.

HARPER, J. F. 1972 The motion of bubbles and drops through liquids. *Adv. Appl. Mech.* **12**, 59–129.

HNAT, J. G. & BUCKMASTER, J. D. 1976 Spherical cap bubbles and skirt formation. *Phys. Fluids* **19**, 182–194.

HUA, J. & LOU J. 2007 Numerical simulation of bubble rising in viscous liquid. *J. Comput.* Phys. **222**, 769–795.

JOHNSON, A. & WHITE, D. B. 1991 Gas-rise velocities during kicks. *SPE Drilling Engineering,* **6**, 257–263, and *Society of Petroleum Engineers Paper* 20431.

KARAPETSAS, G. & TSAMOPOULOS, J. 2006 Transient squeeze flow of viscoplastic materials. *J. Non-Newtonian Fluid Mech.* **133**, 35–56.

KOH, C. & LEAL, L. G. 1989 The stability of drop shapes for transition at zero Reynolds number through a quiescent fluid. *Phys. Fluids* A **1**, 1309–1313.

LEVICH, V. G. 1949 The motion of bubbles at high Reynolds numbers. *Zh. Eksper. Teor. Fiz.* **19**, 18–24.

LIU, B. T., MULLER, S. & DENN, M. M. 2002 Convergence of a regularization method for creeping flow of a Bingham material about a rigid sphere, *J. Non-Newtonian Fluid Mech.* **102**, 179–191.

MAGNAUDET, J. & EAMES, I. 2000 The motion of high-Reynolds-number bubbles in inhomogeneous flows. *Annu. Rev. Fluid Mech.* **32**, 659–708.

MALAGA, C. & RALLISON, J. M. 2007 A rising bubble in a polymer solution. *J. Non-Newtonian Fluid Mech.* **141**, 59–78.

MAXWORTHY, T., GNANN, C., KURTEN, M. & DURST, F. 1996 Experiments on the rise of air bubbles in clean viscous liquids. *J. Fluid Mech.* **321**, 421–441.

MIKSIS, M. J., VANDEN-BROECK, J. M. & KELLER, J. B. 1982 Rising bubbles. *J. Fluid Mech.* **123**, 31–41.

MOORE, D. W. 1963 The boundary layer on a spherical gas bubble. *J. Fluid Mech.* **16**, 161–176.

MOORE, D. W. 1965 The velocity of rise of distorted gas bubbles in a liquid of small viscosity. *J. Fluid Mech.* **23**, 749–766.

PAPANASTASIOU, T. C. 1987 Flows of materials with yield. *J. Rheol.* **31**, 385–404.

PILZ, C. & BENN, G. 2007 On the critical bubble volume at the rise velocity jump discontinuity in viscoelastic liquids. *J. Non-Newtonian Fluid Mech.* **145**, 124–138.

RYBCZYŃSKI, W. 1911 On the translatory motion of fluid sphere in a viscous medium. *Bull. Intl l' Acad. Polonaise Scie. Lett. Classe des Sciences Mathématiques et Naturelles* A, 40–46.

RYSKIN, G. & LEAL, L. G. 1984 Numerical solution of free-boundary problems in fluid mechanics. Part 2. Buoyancy-driven motion of a gas bubble through a quiescent liquid. *J. Fluid Mech.* **148**, 19–35.

SCHENK, O. & GÄRTNER, K. 2004 Solving unsymmetric sparse systems of linear equations with PARDISO. *J. Future Generations Computer Systems* **20**, 475–487.

SCHENK, O. & GÄRTNER, K. 2006 On fast factorization pivoting methods for symmetric indefinite systems. *Elec. Trans. Numer. Anal.* **23**, 158–179.

SMYRNAIOS, D. & TSAMOPOULOS, J. 2001 Squeeze flow of Bingham plastics. *J. Non-Newtonian Fluid Mech.* **100**, 165–190.

STEIN, S. & BUGGISCH, H. 2000 Rise of pulsating bubble in fluids with a yield stress. *Z. Angew. Math. Mech.* **11–12**, 827–834.

TAYLOR, T. & ACRIVOS, A. 1964 On the deformation and drag of a falling drop at low Reynolds number. *J. Fluid Mech.* **18**, 466–476.

TERASAKA, K. & TSUGE, H. 2001 Bubble formation at a nozzle submerged in viscous liquids having yield stress. *Chem. Engng Sci.* **56**, 3237–3245.

UNVERDI, S. O. & TRYGGVASON, G. 1992 A front tracking method for viscous, incompressible, multi-fluid flows. *J. Comput. Phys.* **100**, 25–37.